Characterization of precipitating clouds by ground-based measurements with the triple-frequency polarized microwave radiometer ADMIRARI

Alessandro Battaglia [*]

Meteorological Institute, University of Bonn, 53121 Bonn, Germany

Pablo Saavedra

Meteorological Institute, University of Bonn, 53121 Bonn, Germany

Thomas Rose

Radiometer Physics GmbH, Meckenheim, Germany

Clemens Simmer

Meteorological Institute, University of Bonn, 53121 Bonn, Germany

---

[*] *Corresponding author address:* Auf dem Hugel, 20, 53121 Bonn, Germany.

E-mail: batta@uni-bonn.de

Abstract

A groundbreaking new-concept multi-wavelength dual-polarized ADMIRARI (ADvanced Microwave Radiometer for Rain Identification) radiometer has been built and continuously operated in two field campaigns (COPS and EUCAARI). The radiometer has 6 channels working in horizontal and vertical polarization at 10.6, 21.0 and $36.5\ GHz$ and it is completely steerable both in azimuth and in elevation. Its main advantage is represented by its capability of being operated in rainy conditions and of retrieving simultaneously water vapor, rain and cloud liquid water paths via a Bayesian retrieval scheme. We use many realizations of the Goddard Cumulus Ensemble model to establish a prior probability density function of rainfall profiles. Detailed three-dimensional radiative transfer calculations, which account for the presence of non-spherical particles in preferential orientation, simulate the downwelling brightness temperatures and establish the similarity of radiative signatures and thus the probability that a given profile is actually observed. Particular attention is devoted to the sensitivity of the ADMIRARI signal to 3D effects, raindrops size distribution and axial ratio parameterizations. The polarization and multi-frequency signals represent key information in order to separate the effect introduced by non-Rayleigh scatterers and to separate the rain from the cloud component.

Long-term observations demonstrate that observed brightness temperatures and polarization differences can be well interpreted and reproduced by simulated ones for all three channel simultaneously. Rough estimates of $r-LWP$ derived from colocated observations with a micro rain radar confirm the rain/no rain separation and the variability trend of $r-LWP$ provided by the radiometer-based retrieval algorithm. With this work we demonstrate the potential of ADMIRARI to retrieve information about the rain/cloud partitioning for Midlatitude precipitation systems; the future work on this instrument will provide crucial feedbacks for cloud modelers towards a better characterization of rain

processes.

1. Introduction

Ground-based MW radiometry is a fairly established technique to retrieve vertically-integrated cloud liquid water path ($c - LWP$ hereafter) with dual-channel radiometers (see Westwater (1978); Liljegren et al. (2001); Crewell and Löhnert (2003); Westwater et al. (2004); Rose et al. (2005)), and water vapour and temperature profiles with multi-frequency radiometers (see Solheim et al. (1998); Janssen (1996); Crewell et al. (2001); Löhnert et al. (2008, 2009)). Ground based observations are known to be the most accurate method to observe total liquid water path (LWP) of optically thick cloud with an estimated accuracy of up to $15\ g/m^2$ (Crewell and Löhnert 2003). Above about $300\ g/m^2$, however, clouds generally contain raindrops that

1. may wet the receiving antenna, thus producing absorption losses directly at the antenna window or at the reflector plate used to redirect the radiation into the radiometer feed window. The contamination affects the observed brightness temperatures (T_Bs) to an extend, which depends on rain rate, design of the radiometer and frequency (Jacobson et al. (1986));

2. limit the applicability of the Rayleigh approximation, according to which the extinction coefficient is proportional to the mass of the particles so that the total optical thickness is directly proportional to the LWP. Cloud droplets produce a different mass extinction coefficient than raindrops because in the Mie-resonance region (i.e. size parameter lower than 3 for the specific application) the extinction cross sections remain above their Rayleigh counterpart. Therefore, the same LWP appears “brighter” (i.e. produces higher T_Bs) when the rain component is predominant. For instance, Czekala et al. (2001b) showed that a $1 - km$ thick cloud containing a total $LWP = 1\ kg/m^2$ with different rain/cloud partitioning can produce T_Bs in the range $60 - 130 K$ when observed by a ground based radiometer looking at 30^o elevation angle. Similar results are presented in Sect. 3 of Sheppard (1996).

As a direct implication, in LWP retrieval the rms and bias errors strongly increase in presence of rain and can easily be higher than $100\ g/m^2$ even for total LWP less than $1\ kg/m^2$ (see sect. 5 in Löhnert and Crewell (2003) and sect. 4 in Sheppard (1996)).

The first issue has been addressed either by using spinning reflectors (Jacobson and Nunnelee (1997)), shutters connected to rain sensors (Crewell et al. (2001)) or by introducing hydrofobic coatings on the antennas (Marzano et al. (2005a)) or by adopting a combination of slant viewing angle configuration and fans (Liu et al. (2001)). In order to relieve the second limitation and to resolve the ambiguity introduced by raindrops two main methodologies have been proposed.

a. Polarization studies

Czekala et al. (2001b) suggested to measure the polarization signal $PD \equiv T_{Bv} - T_{Bh}$ which is related to the raindrop size. Large raindrops have non-spherical shapes due to surface tension, internal hydrostatic pressure and friction stress (e.g. Chuang and Beard (1990)) and can be modelled, on average, as oblate spheroids with axial ratio lower than one (parameterisations provided by e.g. Andsager et al. (1999)). Radiative transfer computations performed by Czekala and Simmer (1998) have shown that T_Bs are only marginally affected by raindrop shape while the polarization differences (PDs) are strongly influenced by it. In particular for down-welling radiation [for up-welling radiation (satellite view)the signal is less interpretable due to interferences by variable ice particle amount, e.g. Czekala and Simmer (2002)], the PDs change from small positive values (when spherical raindrops are considered) to large negative values in case of non-spherical particles. The polarization signal can therefore be adopted as a strong signatures of the presence of raindrops and can help in the discrimination of $c - LWP$ and rain liquid water path ($r - LWP$).

Few ground-based polarized measurements at MW frequencies have been documented in literature, like those performed with a $19.2\ GHz$ dual polarization radiometer at $30°$ elevation angle in Southern Germany during 5 months in 1996 and continuously from November 1998 to December

1999 (see Czekala et al. (2001a) for details). The mean PD observations (with corresponding standard deviation) sorted according to the T_B values show a typical signal: PD decreases to negative values with increasing T_B; then the PD saturates at largest negative values around $200\,K$, and finally increases back towards zero for $T_B > 220\ K$. The same authors showed that, in order to explain these signatures, it is necessary to introduce non-spherical partially oriented raindrops. Although the acquired dataset is quite large (513 observation days), the lack of other remote sensing instruments at the measurement site was a major obstacle for the conclusive interpretation of the results.

Similar measurements but of much smaller extent have been presented already by Kutuza et al. (1998), which also confirmed the presence of negative polarization in rain. Troitsky et al. (2003) have analyzed data acquired by a two frequency ($85\ GHz$ and $37\ GHz$) dual polarized ground based radiometer looking at a zenith angle of $65°$ during the Alliance Icing Research Project held in Ottawa in the winter 1999/2000. Their observations refer, however, to snowy condition and are more suited for mixed-phase hydrometeor studies. In their study, the polarization signatures are related to the ice water path and to the microphysics of crystal particles and not to the differential emission/absorption typical of raindrops.

b. Multispectral studies

Other authors (Sheppard (1996); Liu et al. (2001); Marzano et al. (2002, 2005b, 2006); Mätzler and Morland (2008)) have focused on the potential of multi-wavelength ground-based radiometer observations in retrieving integrated rain contents of precipitating clouds. Sheppard (1996) showed agreement between radiometric measurements at 20, 31 and $52\ GHz$ and model computations with a standard error around $4 - 7\ K$. Liu et al. (2001) used a dual-frequency system ($19 - 22\ GHz$) with a very poor angular resolution ($25°$) and showed that for this setup one hour is the optimal averaging period when comparing radiometric-derived and gauge-measured rain rates. Marzano et al. (2002, 2005b, 2006) developed different physically-based retrieval algorithms (based on multiple regression, on a statistical inversion driven by a principal component analyses and on a neural network approach, respectively), applied them to different combinations of multi-frequency ground-based measurements and compared these with rain gauges data (they used typically $30-min$ accumulated values). Such comparisons are, however, plagued by the internal weakness that the atmospheric opacity structure coupled with the non-linearity of the radiation signal has a vastly different temporal and spatial scale than the point-like and time-integrated gauge data. Marzano et al. (2006) therefore presented a more favorable comparison between rain path-attenuations directly derived from the 18.7, 39.6 and $49.5\ GHz$ ITALSAT satellite beacons and the rain amounts retrieved from ground based radiometric measurements at 13.0, 23.8 and $31.6\ GHz$.

Mätzler and Morland (2008) exploited the $31\ GHz$ channel of the TROWARA radiometer to derive rain rates directly from the retrieved optical thickness at this frequency, by using constraints on the rain column derived from radiosonde measurements and the opacity of the atmosphere without rain with the help of other radiometric channels.

The Advanced Microwave Radiometer for Rain Identification (ADMIRARI) has been developed to bridge between the multi-spectral and the polarimetric approach, and to evaluate the additional information content of polarization differences and to assess the accuracy requirements needed for such measurements. The central goal of ADMIRARI observations is a better characterization of the state of the atmosphere in rainy condition, with a particular emphasis on the cloud-rain partitioning. To improve quantitative monitoring of the raining atmosphere has important repercussions in many fields, e.g. in validating the assumed efficiency of cloud to rain conversion in cloud modeling (see introduction in Battaglia et al. (2009)) or in better estimating the effect of the cloud attenuation for high-frequency radars (Pujol et al. (2007)).

After describing the ADMIRARI radiometer design (Sect. 2) and presenting an example of its measurements performed during field campaigns in Sect. 3, the modeling of the ADMIRARI signal via detailed 3D polarized radiative transfer simulations is presented in Sect. 4. The Bayesian retrieval algorithm is discussed and exemplified in Sect. 5. Conclusions and future works are drawn in Sect. 6.

2. Description of the ADMIRARI radiometer

ADMIRARI (see picture in Fig. 1), manufactured by Radiometrics Physics GmbH, has been designed to investigate rain-processes. The main instrument characteristics are summarized in Tab. 1. Additional information can also be found at the ADMIRARI home page *http://www.meteo.uni-bonn.de/forschung/gruppen/admirari/admirari.html*.

The standard atmospheric parameters which can be derived from ADMIRARI observations are the cloud liquid water path ($c-LWP$), the rain liquid water path ($r-LWP$) and the integrated water vapor path (IWV). For this purpose the radiometer comprises in total six channels covering three frequencies (10.65 GHz, 21.0 GHz and 36.5 GHz) and both linear polarizations (H and V). These frequencies have been selected based on different consideration:

- The use of a multi-frequency approach allows a better discrimination of different rain rates. The sensitivity to small amounts of $r-LWP$ is, e.g. significantly better at the higher frequency (see Figs.2-3 in Czekala et al. (2001b)) while high amounts are better monitored at the lower frequency.

- The radiometer should produce the usual dual-channel $IWV-LWP$ product for non-rainy conditions. Therefore one frequency (21.0 GHz with weighting function almost independent of height) has been selected within the weak 22 GHz water vaopor absorption line and the other (36.5 GHz) in the window region beetween this line and the oxygen line complex around $60\,GHz$.

- The three ADMIRARI frequencies mirror those which are/will be present in many space-borne radiometers (e.g. TMI, SSM/I, and GMI). Thus this setup offers an important contribution to the ground-based observations which can be used to validate passive microwave space-borne rain-rate retrieval algorithms.

The general radiometer configuration is illustrated in Fig. 2. For each frequency module the receiver optics consists of a corrugated feed horn with an aperture lens (only at $10.65\ GHz$ the beam is formed by a combination of a corrugated feed horn and an off-axis parabola antenna) which achieves an antenna beam-width of approximately $5°$. The aperture lens (and the $10\ GHz$ parabola antenna) are coated by a water repellent film to avoid the sticking of raindrops on them; they are also equipped with a shield which is effective in protecting the lens from rain when the radiometer is measuring at low elevation angles. The corrugated feed horns offer a low cross polarization level and a rotationally symmetric beam pattern. The Ortho Mode Transducer splits the signal into the V and H polarization component. The ADMIRARI receivers are designed to achieve a high thermal and electrical stability, a compact layout with a minimum of connectors and thermally drifting components, an integrated radiofrequency design, low power consumption and weight. The receivers are based on the direct detection technique (thus no mixers and local oscillators are needed, leading to reduced sensitivity to interfering external signals at down-converted frequencies): as illustrated in the bottom panel of Fig. 2 a Dicke Switch periodically switches the receiver inputs to an internal black body with fixed T_B. This setup continuously determines the system noise temperature of the radiometer. The Dicke Switch is followed by a directional coupler which allows for the injection of a precision noise signal generated by an on/off switching calibrated noise source. This noise signal is used to determine system nonlinearities and system gain drifts during measurements by the “four point” method. A $40\ dB$ low noise amplifier (LNA) boosts the input signal before it is filtered by a waveguide bandpass filter with bandwidth ???? and again boosted by another $20\ dB$ amplifier. Each of the six channels has its own detector diode, which allows for a parallel detection and integration of all channels. The detector outputs are finally amplified by an ultra-low drift operational amplifier chain, AD converted and transmitted to the internal radiometer PC for each of the three frequency modules.

In order to fulfil the requirement of low maintenance regarding absolute calibrations, the receivers are integrated together with their feeds and lenses and are thermally insulated to achieve a high thermal stability with an accuracy of $< 0.05\ K$ over the whole operating temperature range ($-30°C$ to $+40°C$). The system achieves a full internal calibration by using the internal Dicke Switch calibration targets (absolute standards) in combination with the built-in noise injection systems (one for each frequency module) which is used to calibrate the gain drifts. Noise diodes are secondary standards that are calibrated by sky tipping procedures, which can be manually performed during clear sky conditions. A radiometer resolution lower than $0.4°C$ RMS $@1.0\ s$ integration time is achieved with an absolute system stability of $1.0\ K$. The system is fully steerable both in azimuth (0 to $360°$) and in zenith ($-90°$ to $90°$) with azimuthal speed and elevation speed approximately equal to $5°/sec$ and $3°/sec$, respectively. In order to allow easy transportation to campaign sites the whole system is mounted on a trailer.

3. COPS and EUCAARI campaign

During its first life year ADMIRARI participated in the COPS (Wulfmeyer et al. (2008)) and in the EUCAARI campaign (www.knmi.nl/samenw/eucaari/). Measurements obtained during the COPS campaign were already reported in Battaglia et al. (2009). After this first campaign the radiometer design was improved by adding the rain shields and a $24\ GHz$ micro rain radar (MRR) pointing at the same direction as the radiometer (see the black antenna on the right side of Fig. 1).

In the frame of the EUCAARI campaign, ADMIRARI was deployed at the CESAR observatory in Cabauw and has been continuously measuring from the 6^{th} of May to the 1^{st} December 2008. A constant $30°$-elevation observation mode was adopted during the whole campaign. This observation mode will be the focus of the following sections.

The 1^{st} of October 2008 (Fig. 3) can be considered a golden day with a variety of rain events both of stratiform and convective nature. The MRR reflectivity provides an immediate indication about the presence of rain along the slant path observed by the radiometer (the in-build $Z - R$ relationship is ??????). Situations with quite different slant profiles have been present during the day. The T_Bs ($T_B = \frac{1}{2}(T_B^V + T_B^H)$) show a strong correlation with the reflectivity pattern and thus the rain rate (as expected) but with a frequency dependent dynamic range: the $10\ GHz$ channel never exceeds $110\ K$ with a clear-sky baseline around $18\ K$ while $21\ GHz$ ($36.5\ GHz$) T_Bs range between 45 and $273\ K$ (40 and $277\ K$). This is obviously due to the larger opacity of the atmosphere at higher frequencies. Exceptionally high T_Bs are reached around $9\ UTC$.

The polarization differences are negative in presence of rain in agreement with expectations. Extraordinary negative PD values correspond to T_Bs peak at $10\ GHz$ while the two upper frequencies display positive PDs up to $3.5\ K$.

4. Model calculations: spectral and polarization signatures of rainfall

The interaction of MW radiation with clouds and precipitation can be described by the vector radiative transfer equation VRTE (e.g. Haferman (2000)), which can be solved with a range of methodologies (a review is provided by Mätzler (2006)). Large atmospheric hydrometeors tend to have non-spherical shapes (e.g. falling raindrops, snow and other ice crystals) and preferential horizontal orientation. Therefore, hydrometeors represent dichroic media and polarization effects provide specific signatures. Moreover, the combination of scattering effects, the large spatial variation of precipitating hydrometeors in the atmosphere, and the finite beam-width of the radiometers require the consideration of three dimensional effects. Different techniques have been developed to numerically treat the radiative transfer equation for the full Stokes vector in a 3-D environment in the presence of dichroic media (Haferman et al. 1993; Battaglia and Mantovani 2005; Davis et al. 2005). A recent comparison study (Battaglia et al. 2007) has demonstrated that because of its lower computational cost the backward-forward Monte Carlo technique based on importance sampling (Davis et al. 2005) represents the most efficient way to face passive microwave radiative transfer problems related to optically thick 3-D structured clouds including non-spherical preferentially oriented hydrometeors. Therefore, the VRTE has been solved by a backward-forward Monte Carlo scheme, which can also easily account for a finite antenna beam-width. This method represents a major step forward compared to former radiative transfer simulations of rain observations by ground-based radiometers, which always assumed plane parallel atmospheres with spherical hydrometeors and horizontal homogeneity [Sheppard (1996); Marzano et al. (2002, 2005b, 2006)].

a. *Box type cloud model*

In order to quantify the effects of the 3-D structure of a raining cloud on the radiation field sensed by a polarimetric ground-based radiometer, the backward-forward method is applied to a box-type cloud model, as illustrated in Fig. 4. L_x and L_y are the horizontal dimensions of the rain shaft.The cloud box profile is extracted from Cloud Resolving Model (CRM) simulations available from the Goddard Cumulus Ensemble (Tao and Simpson (1993), an example is shown in Fig. 5). Five hydrometeor types are included: rain, cloud water, cloud ice, graupel, and snow. Spherical raindrops are, however, replaced by mass-equivalent horizontally oriented oblate spheroids with axial ratios (lower than 1) parameterized according to Matrosov et al. (2002):

$$\mathcal{A} = 1.0 + 0.05\,b - b\,D_e[cm] \qquad D_e > 0.05\,cm \tag{1}$$

as a function of equivalent spherical raindrop diameter D_e. The shape factor b is equal to 0.6 for equilibrium drop shape. The single scattering properties (i.e. the extinction and the phase matrix, and the emission vector) are computed with a $T-$matrix method according to Mishchenko (2000). The surface is assumed to be Lambertian with emissivity equal to 1.0. Cosmic radiation impinges at $T_c = 2.7\,K$ at the top of the atmosphere.

In order to include $3D$ effects each precipitating profile, characterized by different horizontal extents (varied from $250\ m$ to $8\ km$) is embedded in a clear sky atmosphere (not-shaded region in Fig. 4). The radiances are then simulated as sensed by a radiometer with an antenna beam-width of $5°$ located at different positions either underneath the cloud or at the side of the cloud (the second option is depicted in Fig. 4). The radiative transfer equation is solved according to the backward Monte Carlo technique (Battaglia et al. (2007)). The observation point is indicated by its coordinates (P_x, P_y). Simulated T_Bs and PD_s are depicted in Fig. 6 based on the profile of Fig. 5 for a cloud-box with $L_x = L_y = 4\ km$, keeping P_x fixed at $0.75\ km$. Since the radiometer is sensitive to bulk scattering properties within the whole beam, the rain effect can be sensed by the radiometer even from outside the rain shaft provided that it is operated at sufficiently slanted viewing angles. From pure geometric consideration systems with altitude H are expected to affect the radiometric signal at distances $H/\tan\ \theta_{el}$, θ_{el} being the elevation angle (see Fig. 4). In the T_B plots shown in the right panels of Fig. 6 the homogeneous left upper parts represent regions which are still unaffected by the rain shaft (where also the PDs are zero). On the other hand, even at $6\ km$ distance the $10.6\ GHz$ ($36.5\ GHz$) is affected by the rain cell for elevation angles below $30°$ ($40°$), which translates to an altitude of $3.5\ km$ ($5.0\ km$). This agrees with the structure of the hydrometeor vertical profile shown in Fig. 5 (with the liquid phase confined below $3.5\ km$) and with the different sensitivity of the 10.6 and $36.5\ GHz$ to the ice part of the cloud. Note that strongly negative PDs (e.g. left panels of Fig. 6) can be found for all three frequencies (but at different observing positions and elevation angles); on the other hand slightly positive PDs are obtained only at the higher frequencies.

b. Relevance of 3-D effects

The relevance and role played by 3-D effects in ground-based polarized radiometer observations were discussed in Battaglia et al. (2006). In the present study much more realistic profiles are included with vertical variability of hydrometeor profiles, and with the presence of liquid water and ice particles. 3-D effects are caused by geometrical and by scattering factors (Battaglia et al. 2005, and references therein). For scenarios with weak scattering, $3D$ effects are purely geometrical and the leakages from the radiatively warm side of the cloud can be accounted for by 1-D slant-path (SP) approximation (Liu et al. 1996). As in Sect. 5 of Battaglia et al. (2006) the relevance of "$3D$ scattering effects" is evaluated by using as a reference 1-D SP approximation-based calculations based on the fast RT4 code (Evans and Stephens 1991).

Differences between MonteCarlo and SP RT4 computations become noticeable at $21\ GHz$ and even more at $36.5\ GHz$ as demonstrated in Fig. 7. Two striking features (see points bounded by ellipses) are evident: MonteCarlo produces more negative PDs in the region where the slant optical thickness is roughly around one (see discussion of Fig. 4 in Battaglia et al. (2006)) and slightly positive PDs (up to $3.5\ K$ at $36.5\ GHz$) when the T_B signal is fully saturated (i.e. at large optical thicknesses). The SP RT4 cannot reproduce such large positive PDs at all. These discrepancies are attributable to the deficiencies of the 1-D SP model in computing terms with orders of scattering ≥ 1. Viceversa at the lowest frequency, absorption represents the dominant process so that the predominant term affecting the total signal is the zeroth order of scattering, which is perfectly accounted for by the SP approximation (not shown).

c. *Sensitivity to axial ratio parameterizations and DSD assumptions*

Two factors are expected to play a crucial role in modifying the polarimetric radiometric signal: the axial ratio parameterizations and the DSD assumptions. Drop size distributions are usually modeled according to the exponential Marshall and Palmer distribution $N(D) = N_0 e^{-\Lambda D}$ with $N_0 = 8 \times 10^3 m^{-3}\ mm^{-1}$. In order to account for the departure from this shape we consider hereafter two other DSDs with $N_0 = 4 \times 10^3 m^{-3}\ mm^{-1}$ (so called "thunderstorm") and $N_0 = 32 \times 10^3 m^{-3}\ mm^{-1}$ ("drizzle"). The parametrization of the axial ratio given in Eq. (1) is also modified by allowing variations of the shape factor b from 0.5 to 0.7, which accounts for the observed variability from the equilibrium value [Matrosov et al. (2002)].

Modifications in the DSD assumptions affect the extinction properties of the medium and hence the T_Bs. This can be better understood by looking at the single particle extinction cross section of oblate raindrops (at 30° elevation) per unit volume (top panel of Fig. 8). This quantity exhibits a “super-Rayleigh behavior”, i.e. it remains always higher than the corresponding diameter-independent Rayleigh value (which is identical to the value achieved at small diameters). In fact in the Rayleigh approximation (e.g. for the cloud component) this quantity is expected to be equal to $\frac{6\pi}{\lambda} Im(K)$ (about 0.018, 0.070 and $0.205\ mm^{-1}$ for the three frequencies at $10^\circ C$), λ being the wavelength and $K \equiv \frac{m^2-1}{m^2+2}$ the dielectric factor. From a direct inspection of the the top panel of Fig. 8 it is obvious that such an approximation is valid only for very small droplets with a decreasing range of applicability towards the higher frequencies. Moving out of the Rayleigh region on the left the three frequencies behave differently: while at $10.6\ GHz$ the extinction per unit volume almost always increases with size, it reaches a maximum value around a diameter of 4 and $2.3\ mm$, at 21 and $36.5\ GHz$ respectively. When considering different DSDs (the amount of rain water being the same) we can conclude that at $10.6\ GHz$ DSDs containing large particles produce larger absorption and scattering coefficients (already noticed by Viltard et al. (2000) in their Fig. 2). But this is not always true at the other two frequencies (because of the non-monotonic behavior of the extinction per unit volume curves in Fig. 8). This is highlighted in the bottom panel of Fig. 8 which depicts the $H-$pol extinction coefficients as a function of the $r-LWC$: the thunderstorm DSDs, which favor large raindrops, produce the largest optical thicknesses (hence the highest T_Bs), except at $36.5\ GHz$ at $r-LWC$s larger than $2.5 g/m^3$ where the $M\&P$ is actually the most efficient of the three DSDs in extinguishing radiation. Due to the large relative spread between the three DSDs visible in the bottom panel of Fig. 8, T_Bs at $10.6\ GHz$ will be more heavily affected than at $36.5\ GHz$. Viceversa the axial ratios parametrization variability (in Fig. 8 indicated by the thickness of the line) is not expected to produce any appreciable variability in T_Bs. But it will play a key role in affecting the PDs (see below).

When considering PD effects the larger the raindrops, the higher the dichroism of the medium, the more negative the values attainable by the PDs will be. The same signal will be produced by more prolate raindrops (larger b values). While T_Bs are directly related to the extinction profiles, PDs are driven by other combinations of the scattering properties. Battaglia and Simmer (2007) showed that the following combination of scattering properties (k^{ext} and ϖ are the angular and polarization-dependent extinction coefficient and single scattering albedo, respectively):

$$\Delta\xi(\theta_{el}) \equiv \frac{k_V^{ext}(\theta_{el})[1-\varpi_V(\theta_{el})] - k_H^{ext}(\theta_{el})[1-\varpi_H(\theta_{el})]}{0.5[k_V^{ext}(\theta_{el}) + k_H^{ext}(\theta_{el})]} \tag{2}$$

is relevant when dealing with polarization differences driven by emission/absorption processes (as mainly happening at the ADMIRARI frequencies). As a rule of thumb, at small optical thicknesses, PDs are obtained by multiplying the parameter $\Delta\xi$ by the T_Bs. The parameter $\Delta\xi$ is plotted for $\theta_{el} = 30°$ in Fig. 9 as a function of $r - LWC$ for the lowest and highest ADMIRARI frequency. $\Delta\xi$ is always negative (hence negative PDs) and goes to zero at small $r - LWC$ values (which produce DSDs with mainly spherical particles). The dynamic range attained at $10\ GHz$ is much larger than at $36.5\ GHz$, which suggests the potential for reaching more negative PDs. A strong dependence on the b value is visible (curves with the same symbol are well separated): for instance a thunderstorm rain with a uniform $r - LWC = 2.5\ g/m^3$ producing a $10.6\ GHz\ T_B$ equal to $100\ K$ will roughly produce PD equal to -9.5, -11.5 and $-14\ K$ (see the three black points in the top panel of Fig. 9). The same situation at $36.5\ GHz$ will produce PDs less than half of these. While at $10\ GHz$ DSDs with larger particles (given the same total amount of rain) always produce more negative PDs due to resonance effects, this is not valid any more at $36.5\ GHz$. At this frequency the most efficient DSDs are the thunderstorm, the $M\&P$ and the drizzle roughly for $r - LWC < 0.5\,g/m^3$, $0.5 < r - LWC < 1.5\,g/m^3$ and $r - LWC > 0.5\,g/m^3$ respectively (see arrows in the bottom panel of Fig. 9).

These preliminary considerations have been tested with simulations performed following the methodology described in Sect. 4.a. Profiles with the same total hydrometeor content are hereafter considered; single scattering properties have been computed by assigning the rain content to the three different DSDs and the b parameter to the three value (0.5, 0.6, 0.7). Results of the corresponding radiative transfer computations are shown in Fig. 10. Brightness temperatures (top panels, the $M\&P$ DSD with $b = 0.6$ is taken as a reference) are unchanged by a change in the b value (the simulations with $b = 0.5$ and $b = 0.7$ with the $M\&P$ DSD coincide with the diagonal line) while they are significantly modified by the DSD assumption. The spread is more marked at 10 GHz than at the two highest frequencies and it can be as large as 70 K (see the double arrow in the top left panel of Fig. 10). Note that while at 10 GHz the thunderstorm DSD is always brighter than the other two, at 36.5 GHz when large T_Bs (> 260 K) are encountered (and then, plausibly, large $r - LWC$ as well) the drizzle-type of rain becomes the brightest, which is expected from the previous discussion of the bottom panel of Fig. 8.

Polarization differences (center panels, the $M\&P$ DSD with $b_{eq} = 0.6$ is taken again as a reference) are sensitive both to DSD and to the b parameters. The b dependence is roughly linear (compare the curves labeled with $b = 0.5$ $M\&P$ and $b = 0.7$ $M\&P$ with the diagonal line). A change of ± 0.1 in b produces a decrease/increase in PDs which scales linearly with PDs:

$$PD[b_{eq} \pm 0.1] = PD[b_{eq}](1 \mp \eta_f) \tag{3}$$

with the correction factor η_f equal to about 18.5%, 17.5% and 14.5% respectively for the three frequencies. For instance at 10.6 GHz a $PD = -10$ K produced by assuming $b = 0.6$ will convert to -8.2 and -11.8 K when adopting $b = 0.5$ or $b = 0.7$ respectively. On the other hand the effect of changing DSD is more subtle because the related change in T_Bs will alter the PDs themselves. This can be better understood by considering the $T_B - PD$ space (bottom panels in Fig. 10). A change in the b factor in the range $[0.5 - 0.7]$ will basically produce a pure up and down movement, whose intensity is indicated by the double arrows and will depend on the the given PD level and on the frequency (see different length of the arrows). On the other hand a change in DSD will also produce a right-left shift, e.g. a movement toward right when considering larger raindrops. If the absolute minimum of the $T_B - PD$ curve is already reached, such a movement will push the solution towards a region where PDs actually decrease and therefore will not produce more negative values in the PDs. The bottom panels of Fig. 10 provide a clear picture about the uncertainties we have to contend with in the retrieval problem.

d. Relevance of melting layer effects

Melting hydrometeors are known to be brighter in terms of reflectivities and emissivities, i.e. they have higher backscattering and extinction cross sections than equi-volume raindrops. Battaglia et al. (2003) showed that the description of hydrometeor profiles without explicit use of mixed phased hydrometeors generally underestimate the total optical thickness and the T_Bs. The effect is particularly strong when precipitating systems with low freezing levels are examined, and it is likely to affect more the lower frequencies (see Fig. 8 in Battaglia et al. (2003)), the $10.6\ GHz$ in our specific application. The shape of melting snowflakes has been parameterized e.g. by Russchenberg and Lighthart (1996); Raynaud et al. (2000) in terms of oblate spheroids. These parameterisations were, however, never verified in laboratory experiments so far. This represents a major obstacle for the current study since the axis ratio of melting ice particles drives the PD signal. Developing a model to assess the effect of the melting layer on the ADMIRARI signals is beyond the scope of this work and is left to future investigations.

5. Bayesian retrieval algorithm

Different techniques have been proposed to retrieve rain from ground based radiometry. Marzano et al. (2002, 2005b, 2006) proposed, respectively, a variance-constrained regression, a principal component-based statistical and a neural network retrieval algorithm for rain. Löhnert et al. (2004) presented a more physical direct retrieval for deriving physically consistent profiles of temperature, humidity, and cloud liquid water content by combining a suite of multi-instrument ground-based observations. All measurements were integrated within the framework of optimal estimation to guarantee a retrieved profile with maximum information content.

Our retrieval technique of integrated water vapor IWV, cloud and rain liquid water path is based upon a Bayesian approach. The three-dimensional vector $\mathbf{x} = [IWV,\, c-LWP,\, r-LWP]$ includes all the physical quantities to be retrieved in the inversion method while the vector $\mathbf{y}_{obs}$ represents the set of available sensor observations (i.e. a 6-dimensional vector with the down-welling T_Bs and PDs at the three ADMIRARI frequencies). We use many realizations of the Goddard Cumulus Ensemble model to establish a prior probability density function of rainfall profiles (and of associated $\mathbf{x}_j, j = 1, \ldots N_{prof},\, N_{prof} \approx 10^6$) . Detailed three-dimensional radiative transfer calculations (as described in Sect. 4) are performed to determine the ADMIRARI simulated observations $\mathbf{y}_{sim}(\mathbf{x}_j)$ relative to the cloud model profiles. For each CRM profile many different positions and cloud thicknesses are considered. It is assumed that the "best" estimate of $\mathbf{x}$, given the set of observations $\mathbf{y}_{obs}$, is the expected value

$$E(\mathbf{x}) = \int\int \ldots \int \mathbf{x}\, pdf(\mathbf{x})\; d\mathbf{x} \tag{4}$$

where the probability density function $pdf(\mathbf{x})$ is proportional to the conditional probability that $\mathbf{x}$ represents the true atmosphere state, $\mathbf{x_{true}}$, given that $\mathbf{y}$ is equal to the observed $\mathbf{y}_{obs}$. When using the large atmospheric profile/radiative database, an estimate of the expected value of Eq. (4) follows as (e.g. Kummerow et al. (1996)):

$$\begin{aligned} \hat{E}(\mathbf{x}) &= \sum_{j=1}^{N_{prof}} \mathbf{x}_j\; w_j \qquad (5) \\ w_j &\equiv \frac{\exp\left\{-0.5\,[\mathbf{y}_{obs} - \mathbf{y}_{sim}(\mathbf{x}_j)]^T\,(\mathcal{O}+\mathcal{S})^{-1}\,[\mathbf{y}_{obs} - \mathbf{y}_{sim}(\mathbf{x}_j)]\right\}}{\sum_{j=1}^{N_{prof}} \exp\left\{-0.5\,[\mathbf{y}_{obs} - \mathbf{y}_{sim}(\mathbf{x}_j)]^T\,(\mathcal{O}+\mathcal{S})^{-1}\,[\mathbf{y}_{obs} - \mathbf{y}_{sim}(\mathbf{x}_j)]\right\}} \end{aligned}$$

where the summation is carried over all model simulated profiles ($\mathbf{x}_j$) in the atmosphere/radiative model database. In Eq. (5) $\mathcal{O}$ and $\mathcal{S}$ are the observation and model error covariance matrices, respectively, which are assumed to be diagonal with $\sigma_{\mathcal{O}}[T_B] = 1\ K$ and $\sigma_{\mathcal{O}}[PD] = 0.5\ K$ and with

$\sigma_{\mathcal{S}}[T_B] = 2\ K$ and $\sigma_{\mathcal{S}}[PD] = \frac{\eta_f}{3}\,|PD|\ \ K$ following the uncertainties related to the shape factor, see Eq. (3). We introduce also a quality index (QI) for assessing the quality of the matching between simulations and observations defined as:

$$QI \ \equiv \ min\left\{[\mathbf{y}_{obs} - \mathbf{y}_{sim}(\mathbf{x}_j)]^T\,(\mathcal{O}+\mathcal{S})^{-1}\,[\mathbf{y}_{obs} - \mathbf{y}_{sim}(\mathbf{x}_j)]\right\} \tag{6}$$

where the minimum is searched over the whole database of simulated profiles. Values of QI lower than 6 indicates that we are fitting all six measurements on average within the model/measurement standard deviation. Values larger than 15/20 indicate a bad agreement between measurements and simulations.

Parallel to the ADMIRARI retrieval we performed a completely independent retrieval for the $r-LWP$ based only on the MRR measurements. Assuming the validity of Rayleigh approximation for the reflectivity and an exponential DSD the relationship between radar reflectivity and $r-LWC$ is provided by:

$$r-LWC[g/m^3] = 7.32e-05 \times (N_0[1/(m^3\,mm)]))^{0.4286} \times (Z[mm^6/m^3]).^{0.5714} \tag{7}$$

which can be integrated over the whole MRR slant path located below the freezing level to get the slant $r-LWP$. In the following we use the Marshall& Palmer value $N_0 = 8\times 10^3\ m^{-3}\ mm^{-1}$ in Eq. (7). The variability of N_0 as introduced in Sect. 4c already accounts for a variation of -25% and $+80\%$ with respect to this selected value. Underestimation of the $r-LWP$ is also introduced by attenuation, which in strong rain damp the measured reflectivity compared to the effective one. A rough estimate of such attenuation at $24.1\ GHz$ is given by:

$$Att[dB/km] = 5.01\times 10^{-4}\ Z[mm^6/m^3]^{0.85}.$$

An example of the retrieval results is provided in Fig. 11, for observations collected in the afternoon of 30^{th} September 2008. Humidity and temperature conditions can be described by an IWP around $25\ \ kg/m^2$, a surface temperature around $10°C$ and a freezing level located close to $2\ \ km$

height. A continuous rain event starting just before $18.0\,UTC$ is here considered. The event is highlighted by negative PDs at all frequencies (center top panel) and by high MRR reflectivities (bottom left panel). The QI (right top panel) shows values almost always lower than 15, indicating that the simulations generally fit the observations. This is also demonstrated in the top left and center panels of Fig. 11 where the measured (continuous line) and closest-to-measured simulated (diamonds) T_Bs and PDs are shown. When reverting to the retrieval products (bottom right panel) there is a quite reasonable agreement between the ADMIRARI Bayesian retrieved slant $r-LWP$ (continuous blue line) and the MRR $Z-$based slant $r-LWP$ (dotted black line). This is obviously not always the case.

The panels in Fig. 12 depict a short ($\approx 10min$) strong convective event. In this case slant $r-LWP$ and $c-LWP$ higher than 4 and $2.5\,kg/m^2$ are retrieved by the algorithm. Note how the onset and the end of the precipitation period (clearly evident in the radar image) is well captured by the radiometer as well. Close to the peak of $r-LWP$ the QI becomes extremely poor. We have to remark that we found a downward misalignment of the $10.6\;GHz$ compared to the other two by 7 degrees. Although this has been accounted for in the retrieval scheme, the mismatch between the slant volume observed by the three channel adds additional uncertainty in the retrieval scheme. Note that this problem explains also the mismatch between the simulated and observed T_Bs during the COPS campaign mentioned in Battaglia et al. (2009).

6. Conclusions and future work

The new-concept multi-wavelength dual-polarized ADMIRARI radiometer has been presented. Its main advantage is represented by its capability of being operated in rainy conditions and of retrieving simultaneously water vapor, rain and cloud liquid water paths. Specifics and characteristics of the sensor together with the Bayesian retrieval scheme and the inherent $3D$ radiative transfer simulations have been described in detail. Extensive observations show that observed brightness temperatures and polarization differences can be well interpreted and reproduced by simulated ones for all three channel simultaneously. Rough estimates of $r - LWP$ derived from colocated observations with a micro rain radar seem to confirm the rain/no rain separation and the variability trend of $r - LWP$ provided by the radiometer-based retrieval algorithm.

Future work envisages to apply the retrieval scheme to all our measurement database in order to produce climatological information about the rain/cloud partitioning for Midlatitude precipitation systems; this will provide ground-breaking feedbacks for cloud modelers towards a better characterization of rain processes. An improved synergy between our radiometer and the MRR is also foreseen via the integration of the range-resolved radar information directly in the retrieval procedure. Finally dedicated studies to well-defined stratiform cases should better characterize the bright band extinction enhancements at the ADMIRARI frequencies, with immediate repercussions in space-borne radiometry application.

1) *

Acknowledgments. The ADMIRARI radiometer and this research has been funded by the *Deutsche Forschungsgemeinschaft* (DFG) under grant BA 3485/1-1. The authors would like to thank the Cabauw site for hosting ADMIRARI during the EUCAARI campaign.

References

Andsager, K., K. V. Beard, and N. S. Laird, 1999: A laboratory study of oscillations and axis ratios for large raindrops. *J. Atmos. Sci.*, **56**, 2673–2683.

Battaglia, A., H. Czekala, and C. Simmer, 2006: Three dimensional effects in polarization signatures as observed from precipitating clouds by low frequency ground-based microwave radiometers. *Atmos. Chem. Phys.*, 4383–4394.

Battaglia, A., C. Davis, C. Emde, and C. Simmer, 2007: Microwave radiative transfer intercomparison study for $3-D$ dichroic media. *J. Quant. Spectrosc. Radiat. Transfer,* **105 (1)**, 55–67, doi:10.1016/j.jqsrt.2006.09.017.

Battaglia, A., C. Kummerow, D.-B. Shin, and C. Williams, 2003: Toward characterizing the effect of radar bright bands on microwave brightness temperatures. *J. Atmos. Ocean. Technol.*, **20 (6)**, 856–871.

Battaglia, A. and S. Mantovani, 2005: Forward Montecarlo computations of fully polarized microwave radiation in non isotropic media. *J. Quant. Spectrosc. Radiat. Transfer*, **95 (3)**, 285–308.

Battaglia, A., F. Prodi, F. Porcu, and D.-B. Shin, 2005: *Measuring Precipitation from space: EURAINSAT and the future*, chap. 3D effects in MW radiative transport inside precipitating clouds: modeling and applications. Kluwer Academic ed., V. Levizzani and P. Bauer and F. J. Turk.

Battaglia, A., P. Saavedra, and C. Simmer, 2009: Rain observations by a multi-frequency dual polarized radiometer. *IEEE Geosci. Rem. Sens. Lett.*, **6 (2)**, 354–358.

Battaglia, A. and C. Simmer, 2007: Explaining the polarization signal from rain dichroic media. *J. Quant. Spectrosc. Radiat. Transfer*, **105 (1)**, 84–101, doi:10.1016/j.jqsrt.2006.11.012.

Chuang, C. and K. V. Beard, 1990: A numerical model for the equilibrium shape of electrified raindrops. *J. Atmos. Sci.*, **47**, 1374–1389.

Crewell, S., H. Czekala, U. Löhnert, C. Simmer, T. Rose, and R. Zimmermann, 2001: MICCY-a 22 channel ground-based microwave radiometer for atmospheric research. *Radio Sci.*, **36**, 621–638.

Crewell, S. and U. Löhnert, 2003: Accuracy of cloud liquid water path from ground-based microwave radiometry. Part II. Sensor accuracy and synergy. *Radio Sci.*, **38 (3)**, doi: 10.1029/2002RS002634.

Czekala, H., S. Crewell, A. Hornbostel, A. Schroth, C. Simmer, and A. Thiele, 2001a: Interpretation of polarization features in ground based microwave observations as caused by horizontally aligned oblate rain drops. *J. Appl. Meteorol.*, **40**, 1918–1932.

Czekala, H., S. Crewell, C. Simmer, and A. Thiele, 2001b: Discrimination of cloud and rain liquid water path by groundbased polarized microwave radiometry. *Geophys. Res. Lett.*, **28 (2)**, 267–270.

Czekala, H. and C. Simmer, 1998: Microwave radiative transfer with nonspherical precipitating hydrometeors. *J. Quant. Spectrosc. Radiat. Transfer*, **60**, 365–374.

———, 2002: On precipitation induced polarization of microwave radiation measured from space. *Meteorologische Zeitschrift*, **11**, 49–60.

Davis, C. P., C. Emde, and R. S. Harwood, 2005: A 3D polarized reversed monte carlo radiative transfer model for mm and sub-mm passive remote sensing in cloudy atmospheres. *IEEE Trans. on Geosci. and Remote Sens.*, **43**, 1096–1101.

Evans, K. F. and G. L. Stephens, 1991: A new polarized atmospheric radiative transfer model. *J. Quant. Spectrosc. Radiat. Transfer*, **46**, 413–423.

Haferman, J. L., 2000: *Light Scattering by Nonspherical Particles: Theory, Measurements, and Applications*, chap. Microwave scattering by precipitation. M. I. Mishchenko, J.W. Hovenier and L.D. Travis, Academic Press, San Diego.

Haferman, J. L., W. F. Krajewski, T. F. Smith, and A. Sanchez, 1993: Radiative transfer for a three-dimensional raining cloud. *Appl. Opt.*, **32**, 2795–2802.

Jacobson, M., D. Hogg, and J. Snider, 1986: Wet reflectors in millimeter-wave radiometry-experiment and theory. *IEEE Trans. Geosci. Remote Sensing*, **GE-24 (5)**, 784 – 791.

Jacobson, M. and W. Nunnelee, 1997: Design and performance of a spinning flat reflector for millimeter-wave radiometry. *IEEE Trans. Geosci. Remote Sensing*, **35 (2)**, 464 – 466.

Janssen, M. A., 1996: *Atmospheric remote sensing by microwave radiometry*. John Wiley & Sons.

Kummerow, C., W. S. Olson, and L. Giglio, 1996: A simplified scheme for obtaining precipitation and vertical hydrometeor profiles from passive microwave sensors. *IEEE Trans. Geosci. Remote Sens.*, **34**, 1213–1232.

Kutuza, B. G., G. K. Zagorin, A. Hornbostel, and A. Schroth, 1998: Physical modeling of passive polarimetric microwave observations of the atmosphere with respect to the third stokes parameter. *Radio Science*, **33 (3)**, 677–695.

Liljegren, J. C., E. E. Clothiaux, G. G. Mace, S. Kato, and X. Dong, 2001: A New Retrieval for Cloud Liquid Water Path Using a Ground-based Microwave Radiometer and Measurements of Cloud Temperature. *J. Geophys. Res.*, **106 (14)**, 14 485–14 500.

Liu, G.-R., C.-C. Liu, and K. T-H, 2001: Rainfall intensity estimation by ground-based dual frequency microwave radiometers. *J. Appl. Meteorol.*, **40**, 1035–1041.

Liu, Q., C. Simmer, and E. Ruprecht, 1996: Three-dimensional radiative transfer effects of clouds in the microwave spectral range. *J. Geophys. Res.*, **101 (D2)**, 4289–4298.

Löhnert, U. and S. Crewell, 2003: Accuracy of cloud liquid water path from ground-based microwave radiometry. Part I. Dependency on cloud model statistics. *Radio Sci.*, **38 (3)**, 8041, doi: 10.1029/2002RS002654.

Löhnert, U., S. Crewell, O. Krasnov, E. O'Connor, and H. Russchenberg, 2008: Advances in continuously profiling the thermodynamic state of the boundary layer: Integration of measurements and methods. *J. Atmos. Ocean. Technol.*

Löhnert, U., S. Crewell, and C. Simmer, 2004: An integrated approach towards retrieving physically consistent profiles of temperature, humidity and cloud liquid water. *J. Appl. Meteorol.*, **43 (9)**, 1295–1307.

Löhnert, U., D. Turner, and S. Crewell, 2009: Ground-based temperature and humidity profiling using spectral infrared and microwave observations: Part 1. Simulated retrieval performance in clear sky conditions. *J. Appl. Meteorol.*, accepted for publication.

Marzano, F., D. Cimini, , and R. Ware, 2005a: Monitoring of rainfall by ground-based passive microwave systems: models, measurements and applications. *Advances in Geosciences*, **2**, 259–265.

Marzano, F., D. Cimini, P. Ciotti, and R. Ware, 2005b: Modeling and measurements of rainfall by ground-based multispectral microwave radiometry. *IEEE Trans. Geosci. Rem. Sens.*, **43**, 1000–1011.

Marzano, F., E. Fionda, and P. Ciotti, 2006: A neural network approach to precipitation intensity and extinction retrieval by ground-based passive microwave technique. *J. Hydrometeor.*, doi.10.1016/j.hydrol.2005.11.42.

Marzano, F. S., E. Fionda, P. Ciotti, and A. Martellucci, 2002: Ground-based multi-frequency microwave radiometry for rainfall remote sensing. *IEEE Trans. Geosci. Rem. Sens.*, **40**, 742–759.

Matrosov, S., K. Clark, B. Martner, and A. Tokay, 2002: X-Band Polarimetric Radar Measurements of Rainfall. *J. Appl. Meteorol.*, **41 (9)**, 941–952.

Mätzler, C., 2006: *Thermal Microwave Radiation - Applications for Remote Sensing*. IET Electromagnetic Waves Series 52, Christian Mätzler, London, UK.

Mätzler, C. and J. Morland, 2008: Advances in surface-based radiometry of atmospheric water. Tech. rep., University of Bern.

Mishchenko, M. I., 2000: Calculation of the amplitude matrix for a nonspherical particle in a fixed orientation. *Appl. Opt.*, **39 (6)**, 1026–1031.

Pujol, O., J.-F.-A. Georgis, L. Feral, and H. Sauvageot, 2007: Degradation of radar reflectivity by cloud attenuation at microwave frequency. *J. Atmos. Ocean. Technol.*, **24 (4)**, 640–657, doi:10.1175/JTECH1992.1.

Raynaud, L., I. Chenerie, and J. Lemorton, 2000: Modeling of radiowave scattering in the melting layer of precipitation. *IEEE Trans. Geo. Rem. Sens.*, **38 (4)**, 1574–1584, doi:10.1109/36.851957.

Rose, T., S. Crewell, U. Löhnert, and C. Simmer, 2005: A network suitable microwave radiometer for operational monitoring of the cloudy atmosphere. *Atmos. Res.*, **75 (3)**, 183–200, doi:10.1016/j.atmosres.2004.12.005.

Russchenberg, H. and L. Lighthart, 1996: Backscattering by and propagation through the melting layer of precipitation: A new polarimetric model. *IEEE Trans. Geosci. Remote Sensing*, **34**, 3–14.

Sheppard, B., 1996: Effect of rain on ground-based microwave radiometric measurements in the 20-90-ghz range. *J. Atmos. Ocean. Technol.*, **13 (6)**, 1139–1151.

Solheim, F. a. J. G., E. R. Westwater, Y. Han, S. Keihm, K. Marsh, and R. Ware, 1998: Radiometric profiling of temperature, water vapor and cloud liquid water using various inversion methods. *Radio Sci.*, **33**, 393–404.

Tao, W. K. and J. Simpson, 1993: Goddard cumulus ensemble model. Part I: Model description. *Terrest. Atmos. Oceanic Sci.*, **4**, 35–72.

Troitsky, A. V., A. M. Osharin, A. V. Korolev, and J. W. Strapp, 2003: Polarization of thermal microwave atmospheric radiation due to scattering by ice particles in clouds. *J. Atmos. Sci.*, **60**, 1608–1620.

Viltard, N., C. D. Kummerow, W. S. Olson, and Y. Hong, 2000: Combined use of the radar and radiometer of TRMM to estimate the influence of drop size distribution on rain retrievals. *J. Appl. Meteorol.*, **39 (12)**, 2103–2114.

Westwater, E. R., 1978: The accuracy of water vapor and cloud liquid determination by dual-frequency ground-based microwave radiometry. *Radio Sci.*, **13**, 667–685.

Westwater, E. R., S. Crewell, and C. Mätzler, 2004: A review of surface-based microwave and millimeter-wave radiometric remote sensing of the troposphere. *Radio Science Bulletin*, **310**, 59–80.

Wulfmeyer, V., A. Behrendt, H.-S. Bauer, C. Kottmeier, U. Corsmeier, A. Blyth, G. Craig, U. Schumann, M. Hagen, S. Crewell, P. D. Girolamo, C. Flamant, M. Miller, A. Montani, S. Mobbs, E. Richard, M. Rotach, M. Arpagaus, H. Russchenberg, P. Schlüssel, M. König, , V. Gärtner, R. Steinacker, M. Dorninger, D. Turner, T. Weckwerth, A. Hense, and C. Simmer, 2008: The convective and orographically-induced precipitation study: A research and development project of the world weather research program for improving quantitative precipitation forecasting in low-mountain regions. *Bull. Amer. Met. Soc.*, doi: 10.1175/2008BAMS2367.1.

List of Figures

FIG. 1. The ADMIRARI radiometer at the CESAR observatory. On the right side (black antenna) a Micro Rain Radar system is installed.

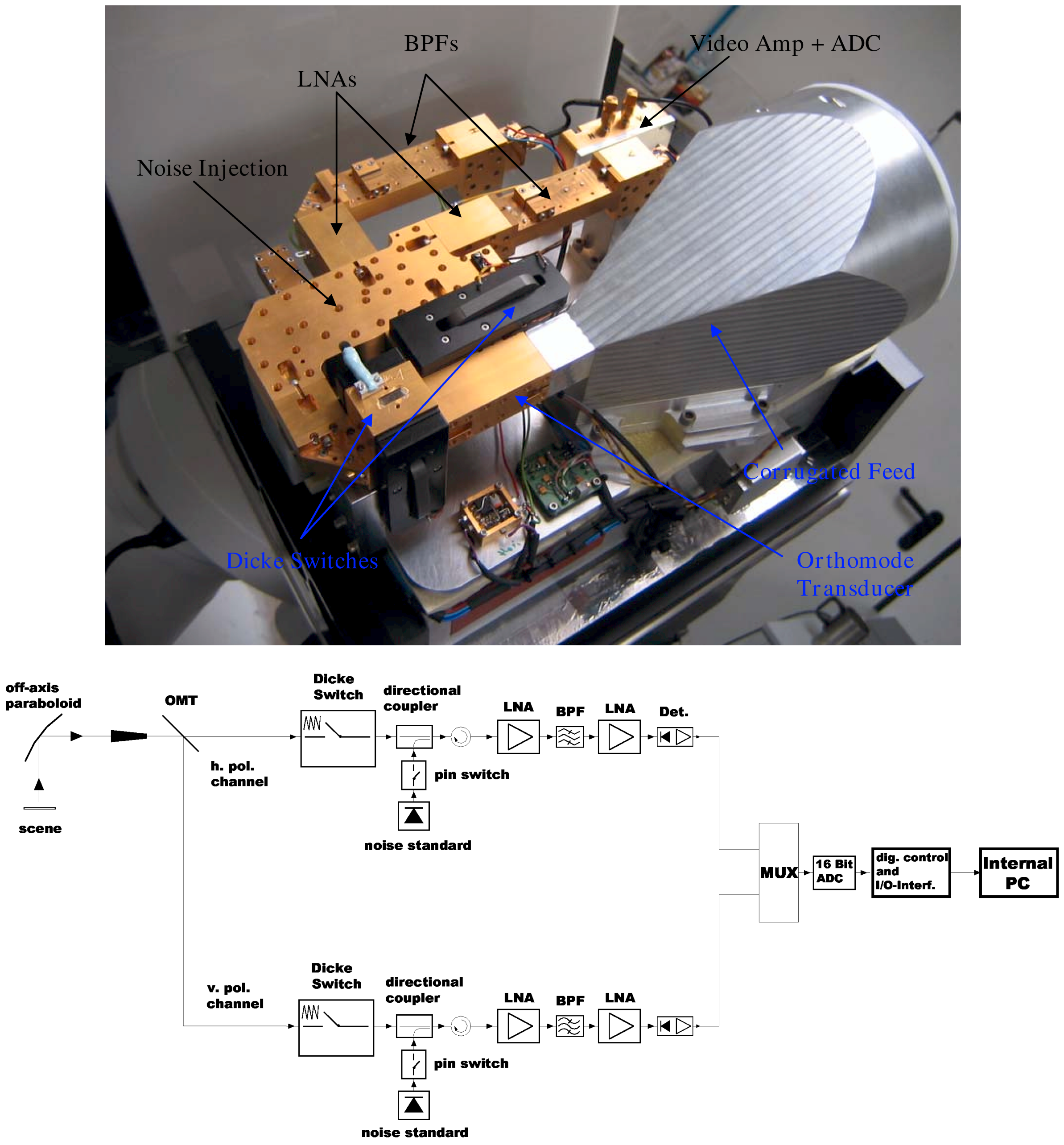

FIG. 2. Picture of the inner radiometer components (top) and a schematic of the receiver layout (bottom). The orthomode transducer is splitting the H and V signals, which are directly detected in two different receiving chains.

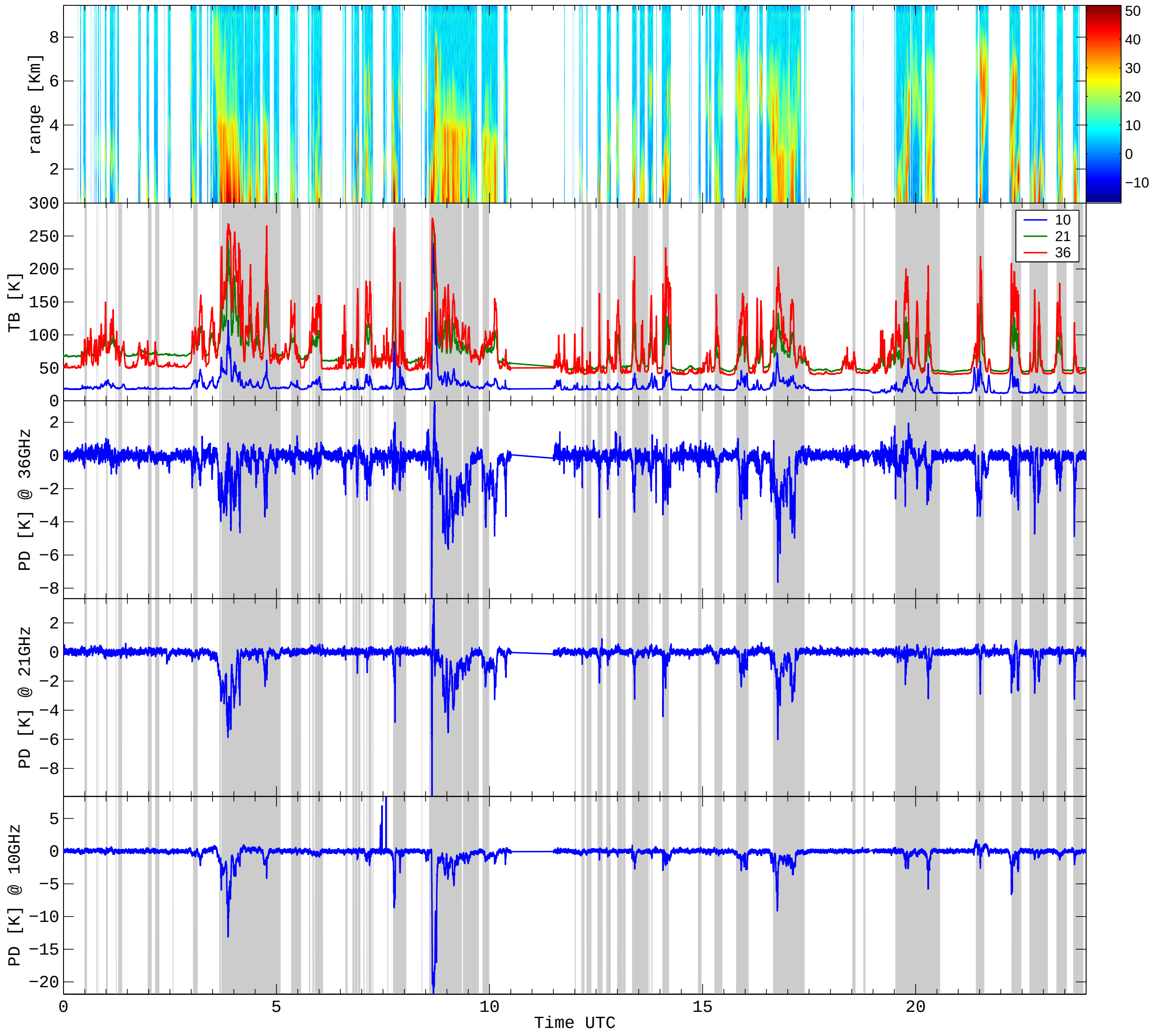

FIG. 3. ADMIRARI measurements during 1/10/2008. From top to bottom: MRR radar reflectivity in dBZ (vertical axis represents range along the slant path), ADMIRARI brightness temperatures ($T_B = \frac{1}{2}(T_B^V + T_B^H)$) and 36.5, 21 and 10.65 GHz polarization differences ($PD = T_B^V - T_B^H$), respectively at $30°$ elevation. Grey intervals indicate rainy periods as sensed by the rain sensor installed on the ADMIRARI trailer.

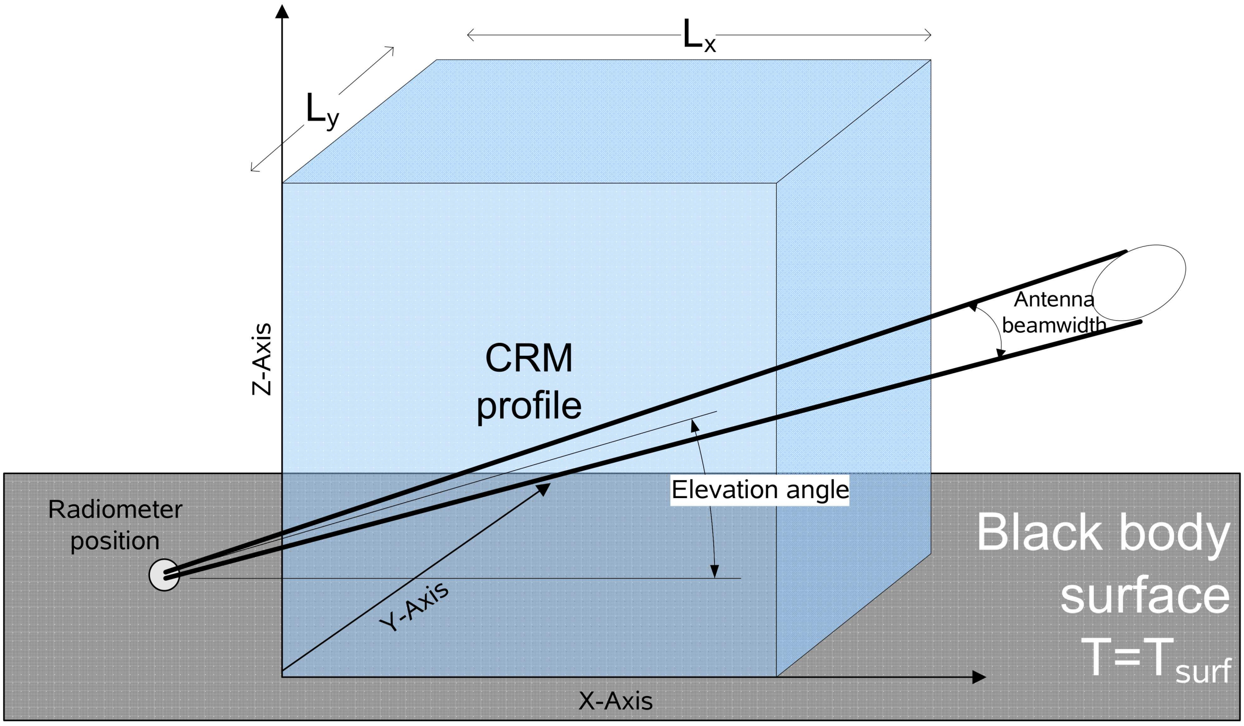

FIG. 4. Schematic for the rain cloud simulation. Radiances have been computed at observation points located at the location $(P_x,\ P_y)$. The blue-shaded area contains the rain system with one vertical hydrometeor and atmospheric profile extracted from a Cloud Resolving Model (like that shown in the Fig. 5). Non shaded areas contain only atmospheric gases; temperature, pressure and humidity profiles are the same as in the blue-shaded area.

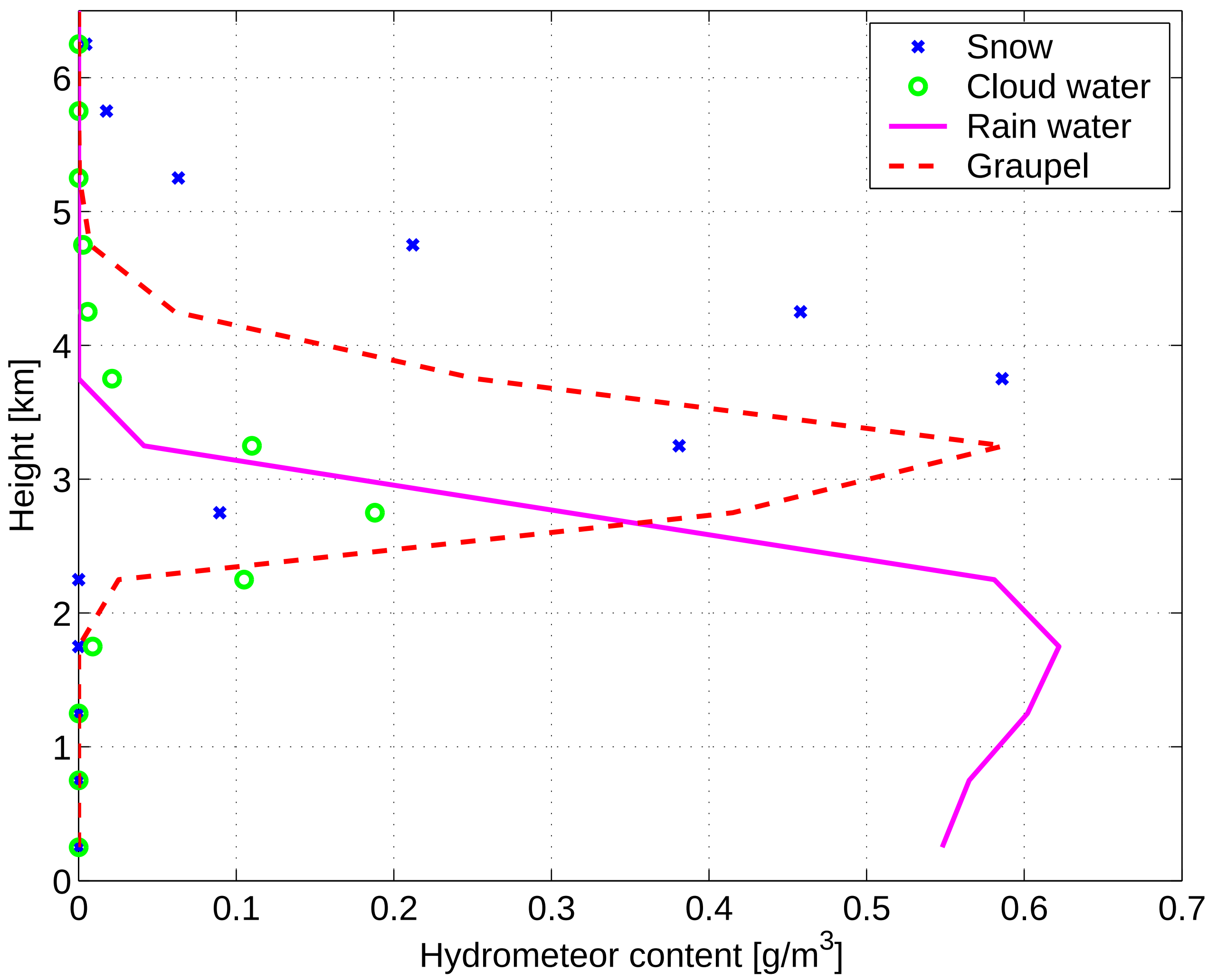

FIG. 5. Example of an hydrometeor profile extracted from a Cloud Resolving Model and adopted in the $3D$ radiative transfer simulations illustrated in Fig. 4.

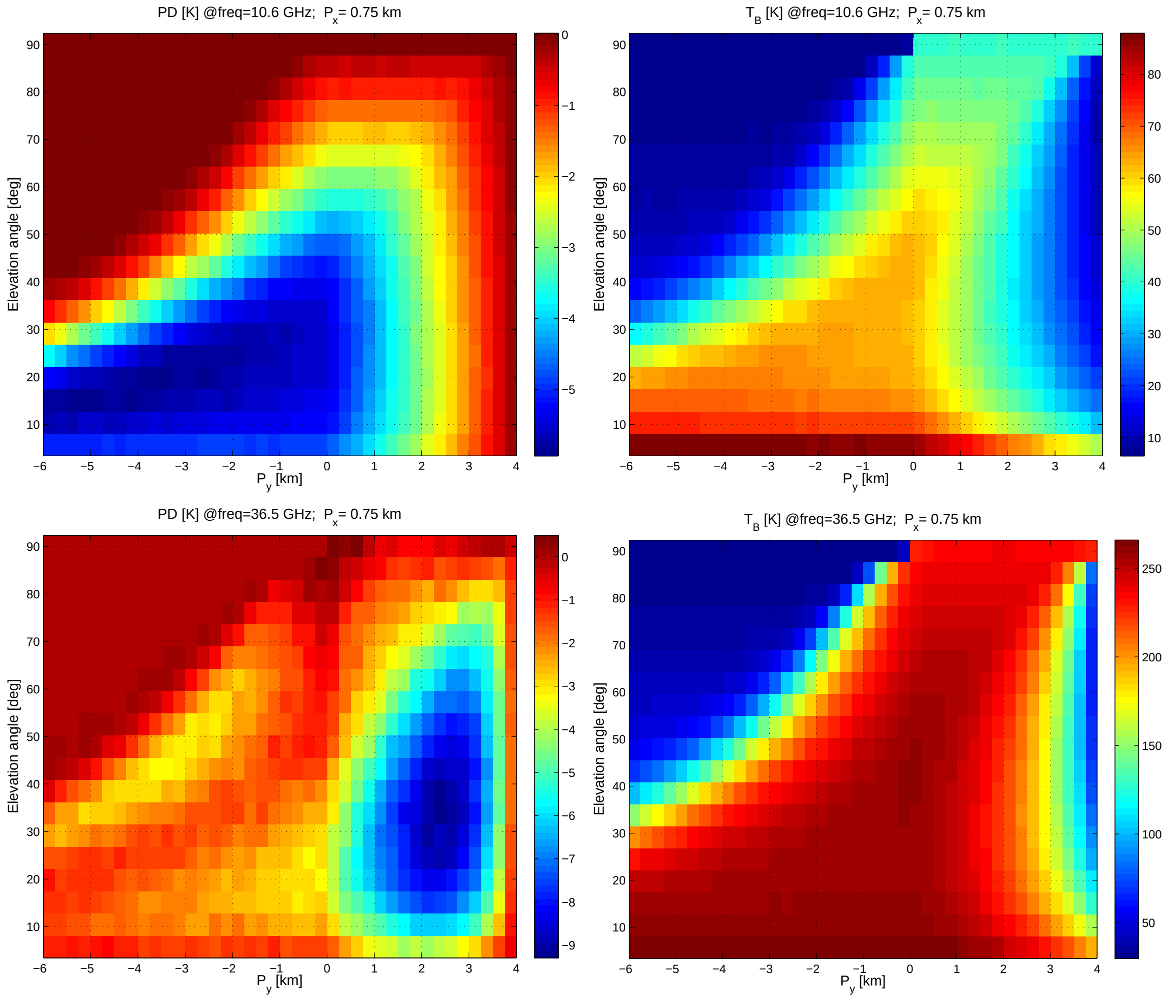

FIG. 6. Polarization differences (left panels) and brightness temperatures (right panels) simulated for the profile of Fig. 5 and the ground-based configuration depicted in Fig. 4 with $L_x = L_y = 4\ km$. The lowest (top) and highest (bottom) ADMIRARI frequencies are considered.

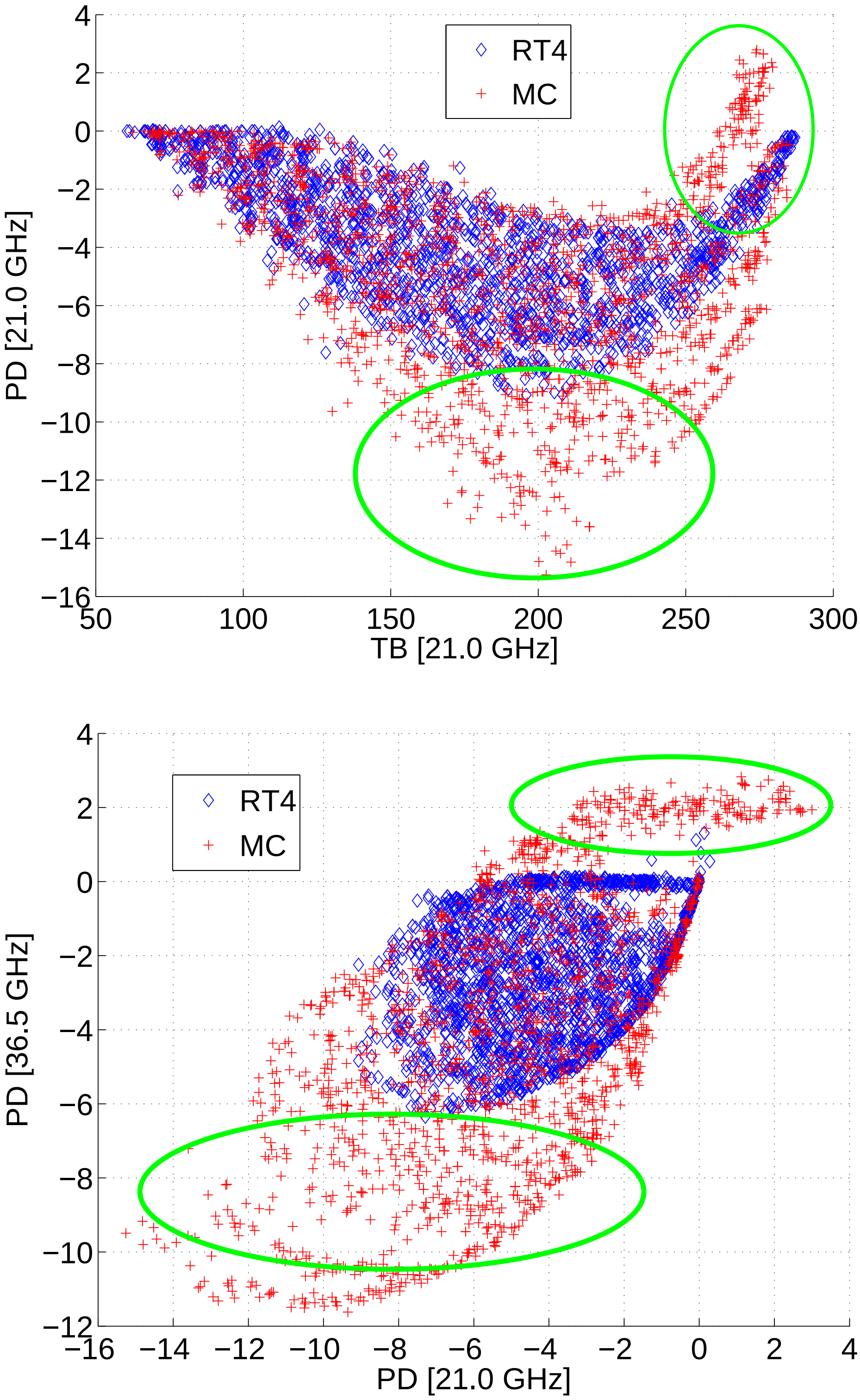

FIG. 7. Scatterplots between SP RT4 and MonteCarlo computations to highlight "3-D scattering effects". The geometry of the simulations is the one illustrated in Fig. 4. with an elevation angle of 30°, $L_x = L_y = 4\ km$ and $P_x = [-3.5 : 1.0 : 3.5]\ km$. About 3000 profiles with freezing levels ranging from 2 to $4\ km$ are considered in this example.

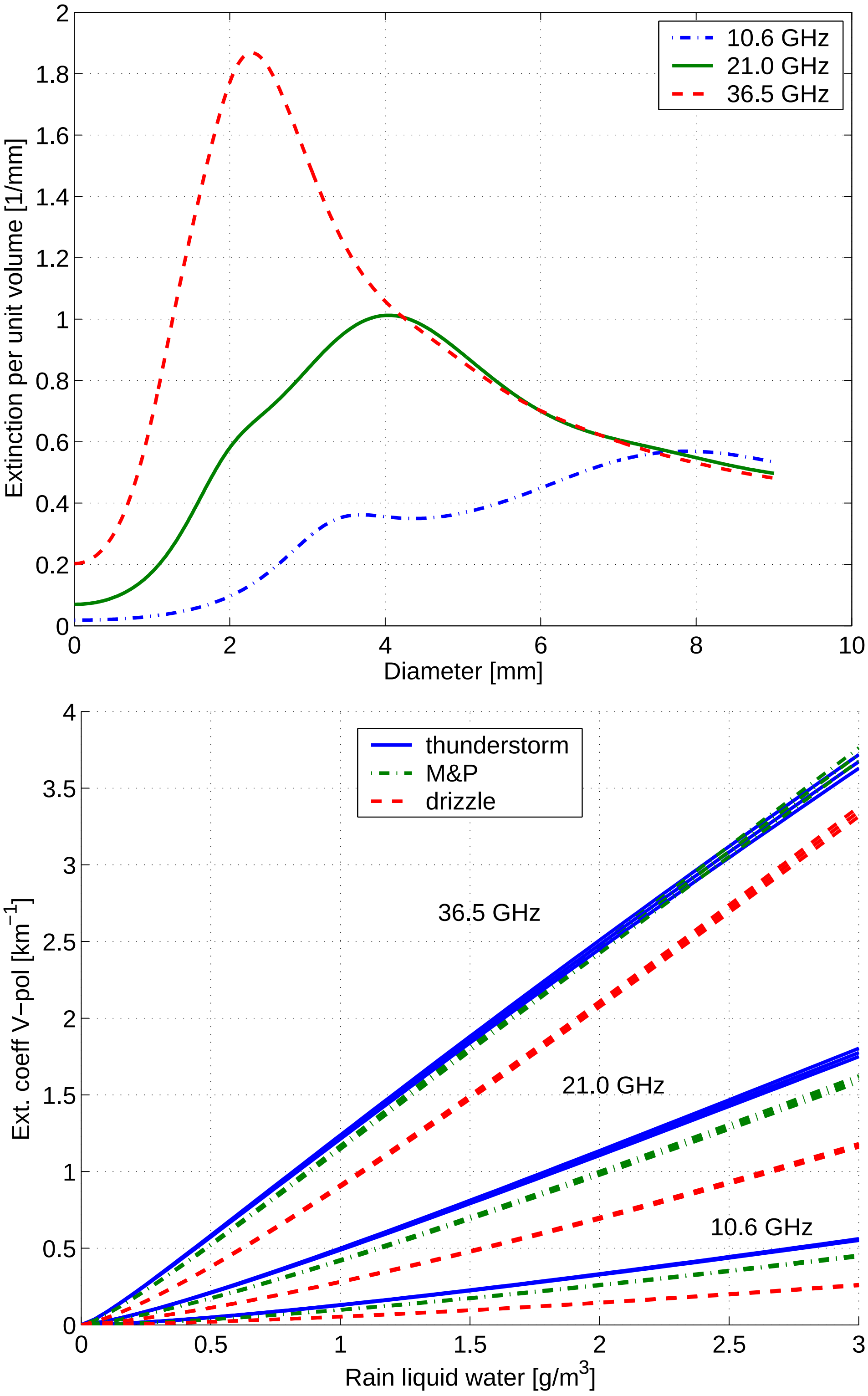

FIG. 8. Top panel:extinction cross section per unit volume in $[mm^2/mm^3]$ as a function of the raindrop equivolume diameter for the three ADMIRARI frequencies. Raindrops up to $9\ mm$ diameter are considered. Bottom: vertical polarization extinction coefficient as a function of the $r-LWC$ in g/m^3 for raindrop populations with three different DSDs as indicated in the legend at the three ADMIRARI frequencies. The thickness of the line accounts for the assumed variability in the coefficient b in Eq. (1) from 0.5 to 0.7.

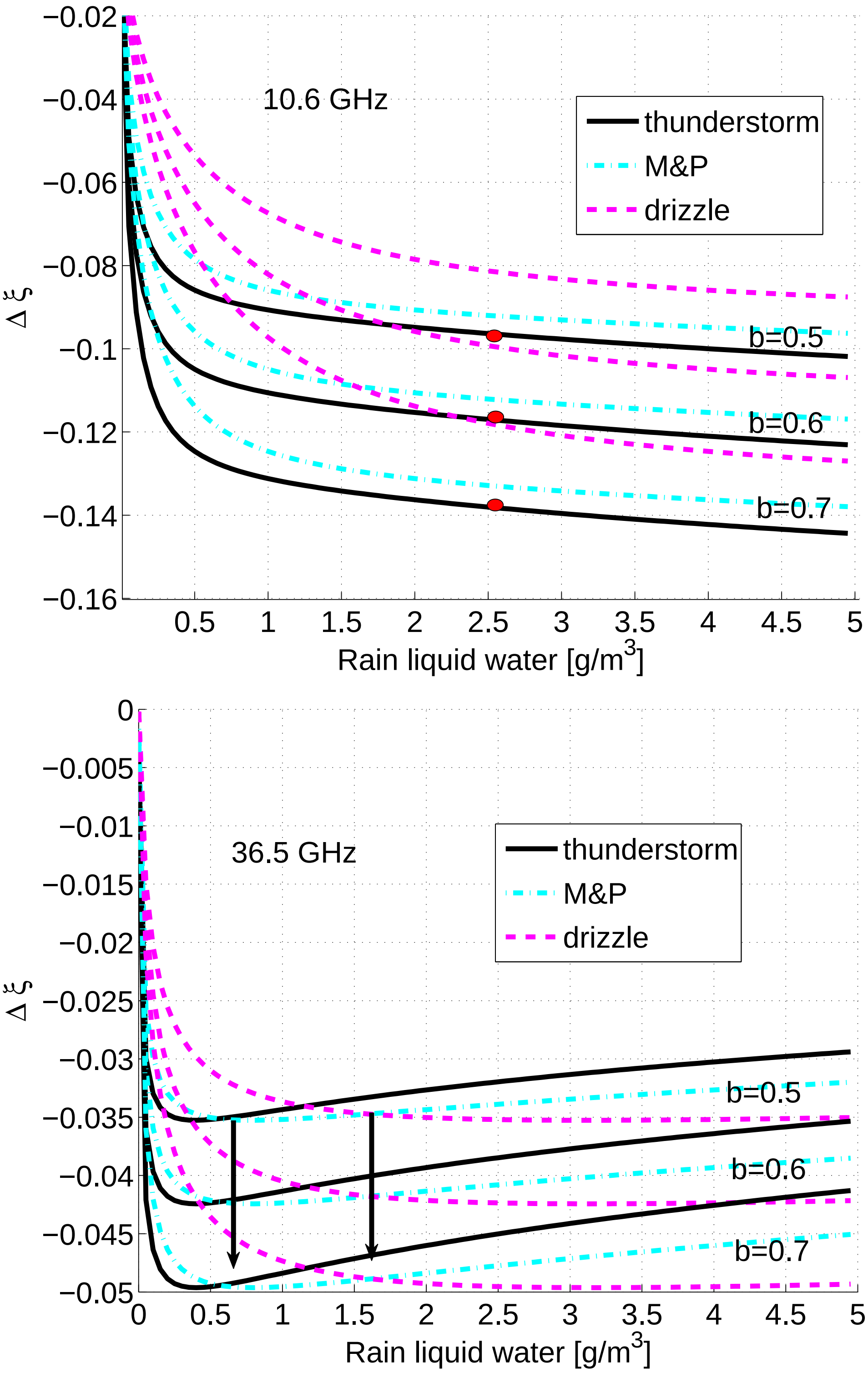

FIG. 9. Parameter $\Delta\xi$ as defined in Eq. (2) evaluated at elevation angle $\theta_{el} = 30^\circ$ at 10.6 (top) and $36.5\ GHz$ (bottom) for three different DSD as a function of the $r - LWC$. Curves plotted with the same style correspond to different b values: 0.5, 0.6 and 0.7 from the top to bottom. See text for details

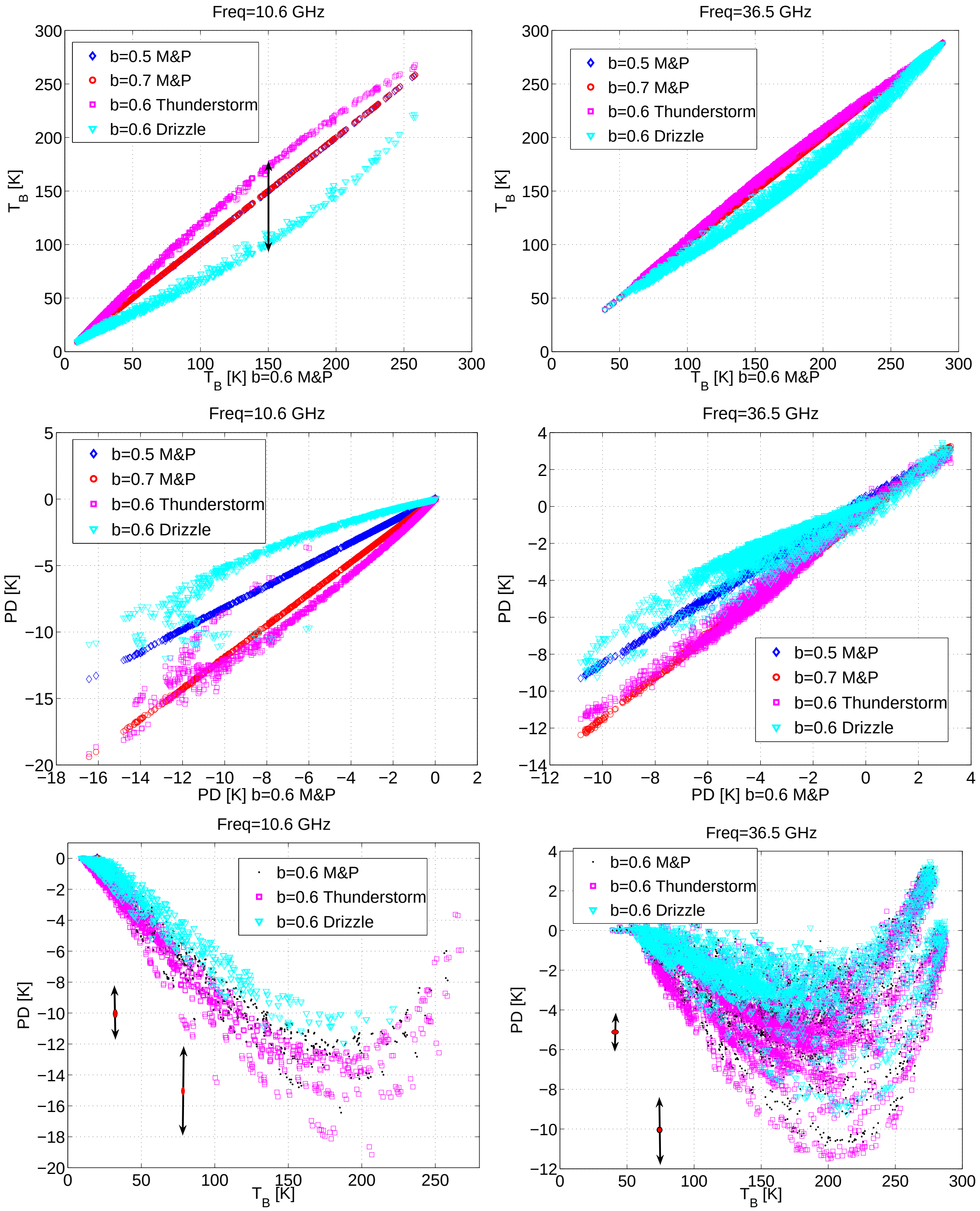

FIG. 10. Simulation study for the sensitivity of T_Bs (top panels) and PDs (center panels) to the DSD and the raindrops axial ratio (see Eq. 1) assumptions. The overall effect in the $T_B - PD$ space is shown in the bottom panels. Only the 10.6 (left) and 36.5 GHz (right panels) ADMIRARI channel are here considered. See text for details.

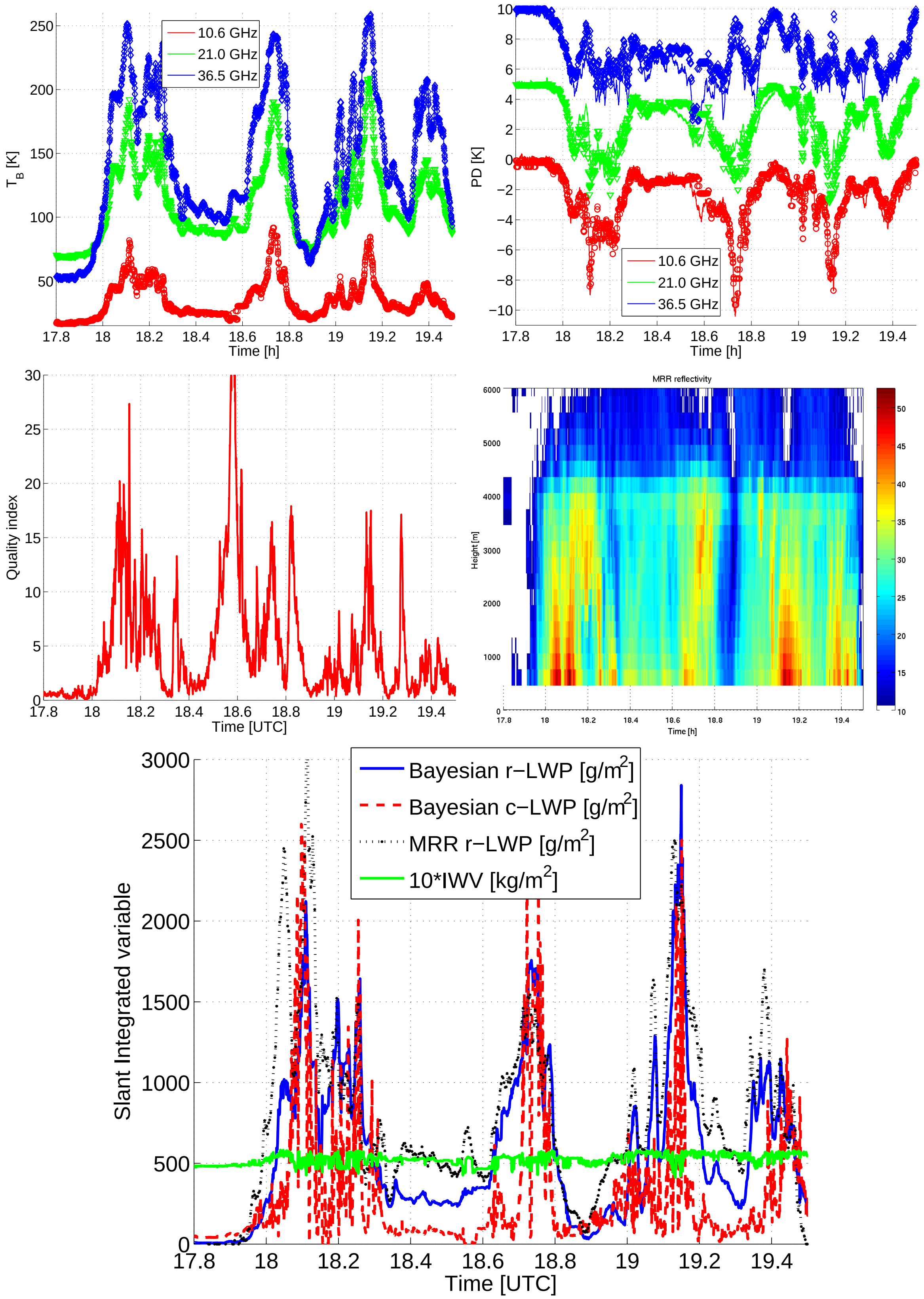

FIG. 11. Case study 30/9/2008 from 17.8 to 19.4.

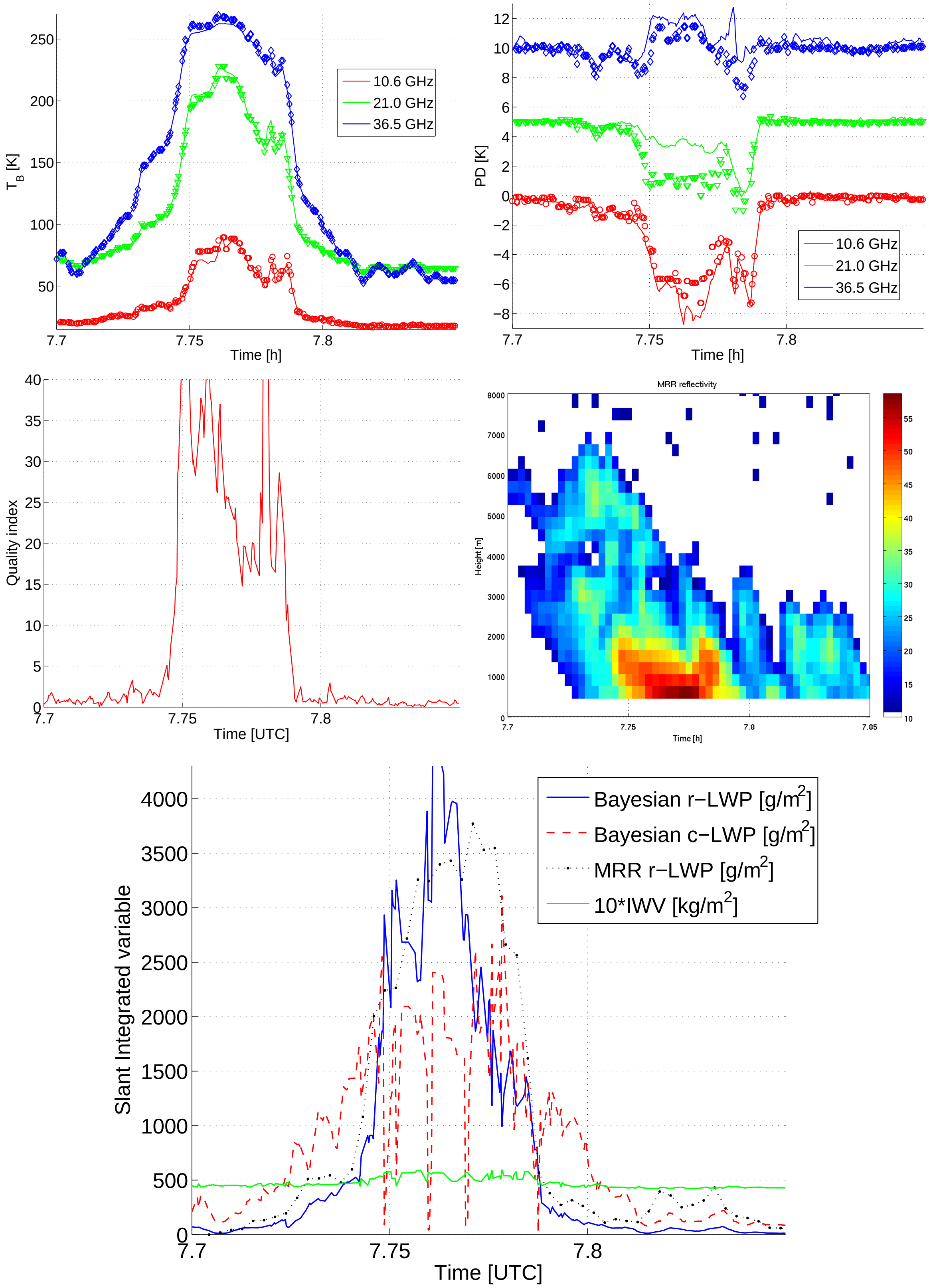

FIG. 12. Case study 01/10/2008 from 7.7 to 7.8.

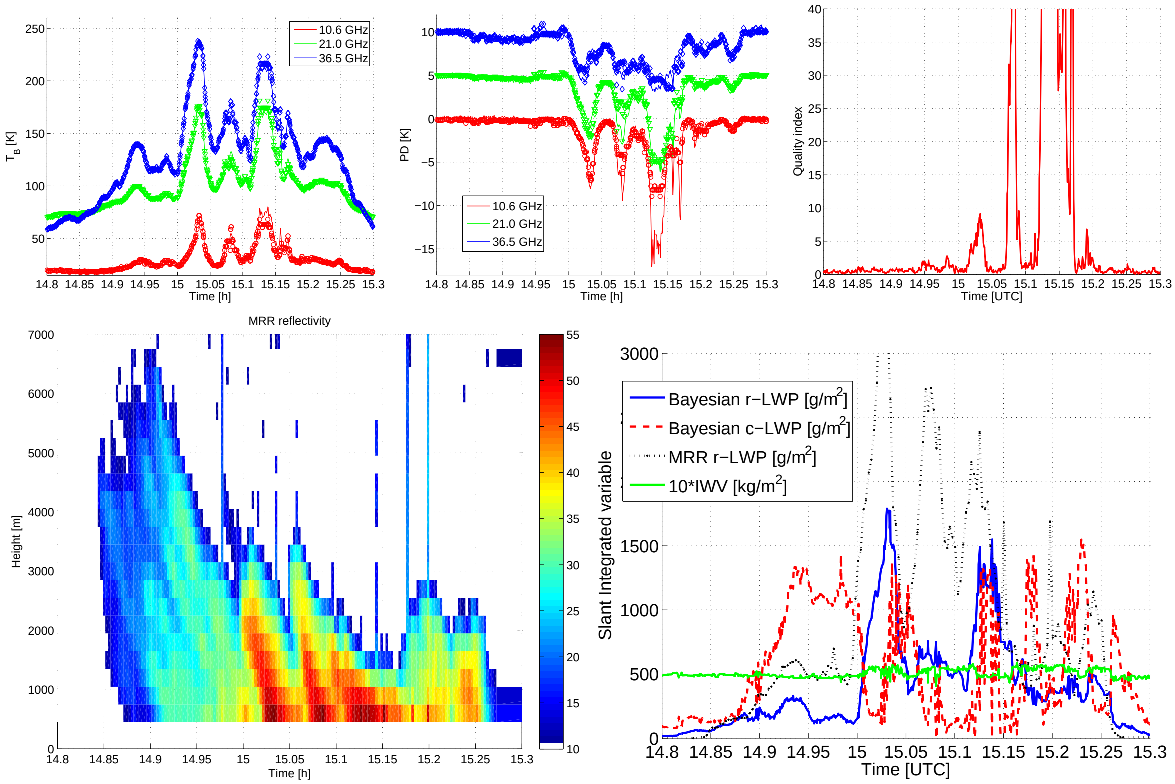

FIG. 13. Case study 3/9/2008 from 14.8 to 15.3.

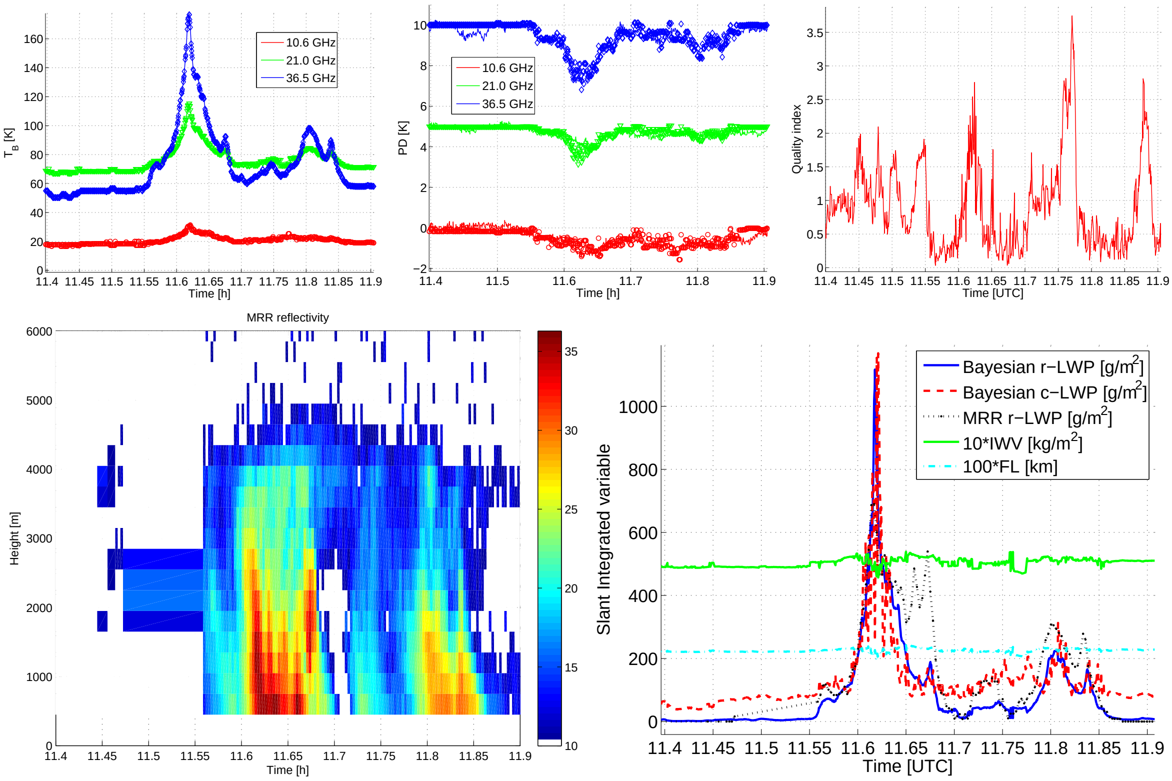

FIG. 14. Case study 30/9/2008 from 11.4 to 11.9.

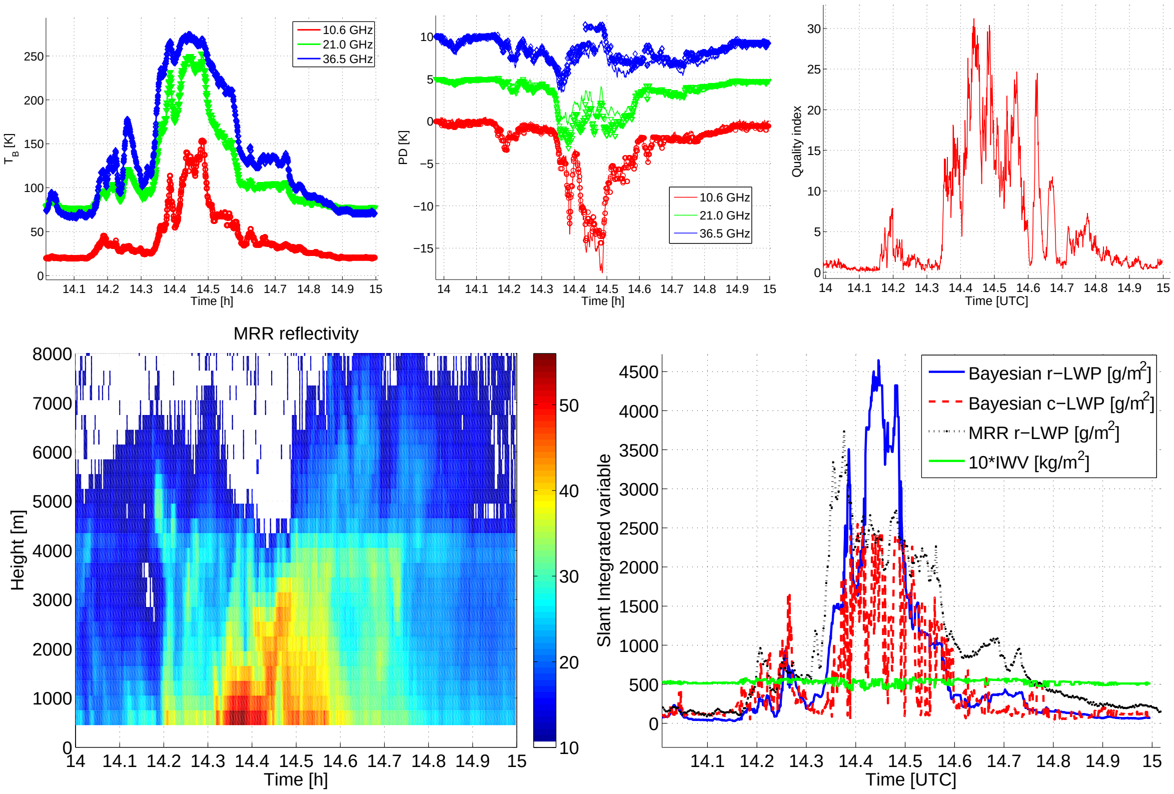

FIG. 15. Case study 30/9/2008 from 14.0 to 15.

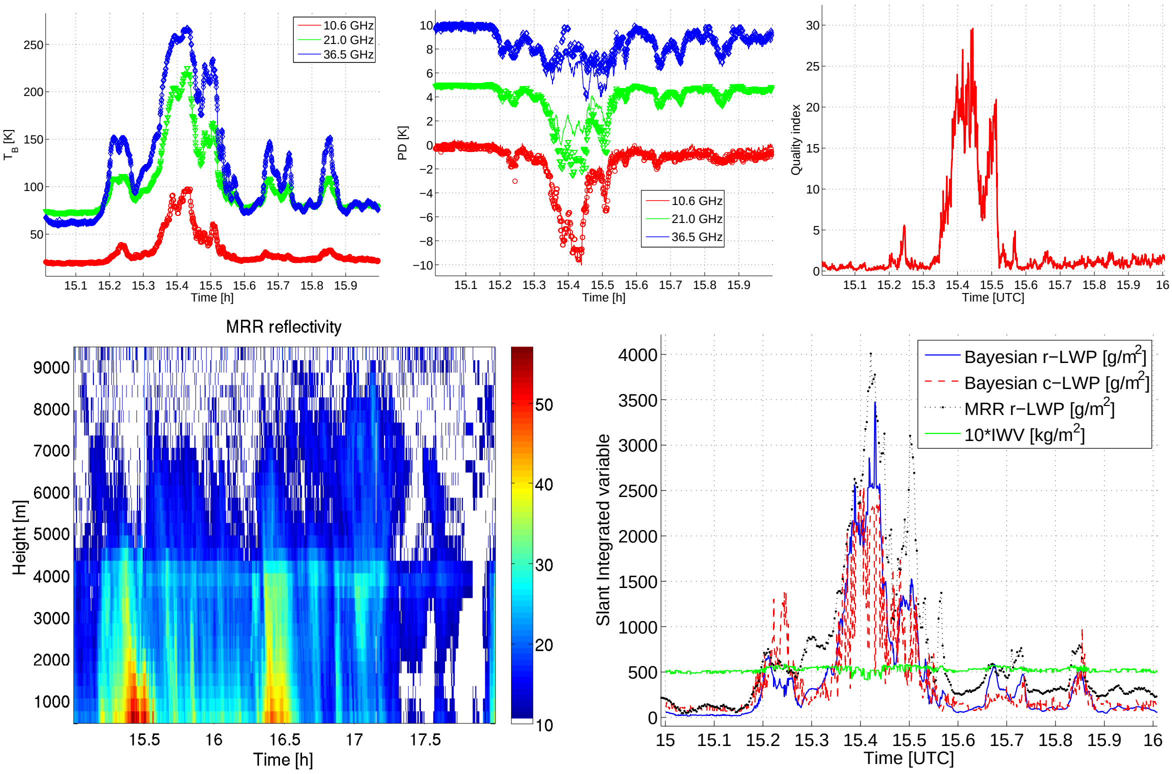

FIG. 16. Case study 30/9/2008 from 15.0 to 16.0.

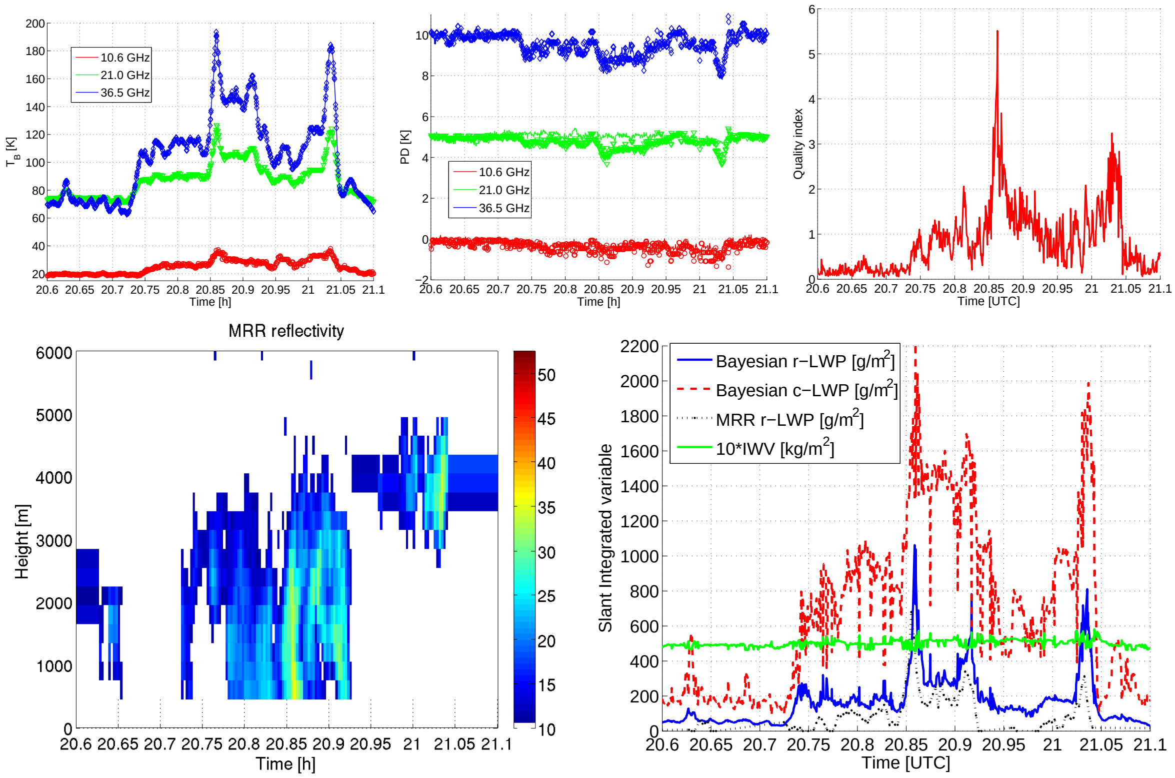

FIG. 17. Case study 30/9/2008 from 20.6 to 21.1.

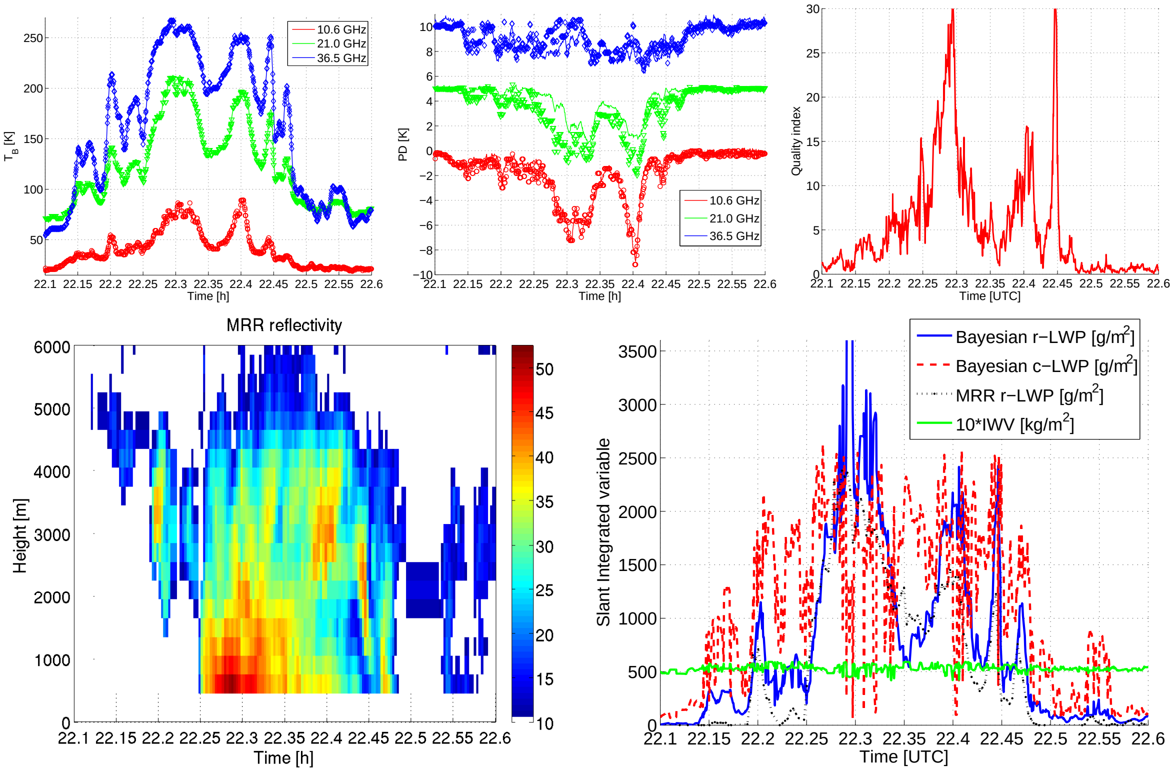

FIG. 18. Case study 30/9/2008 from 22.1 to 22.6.

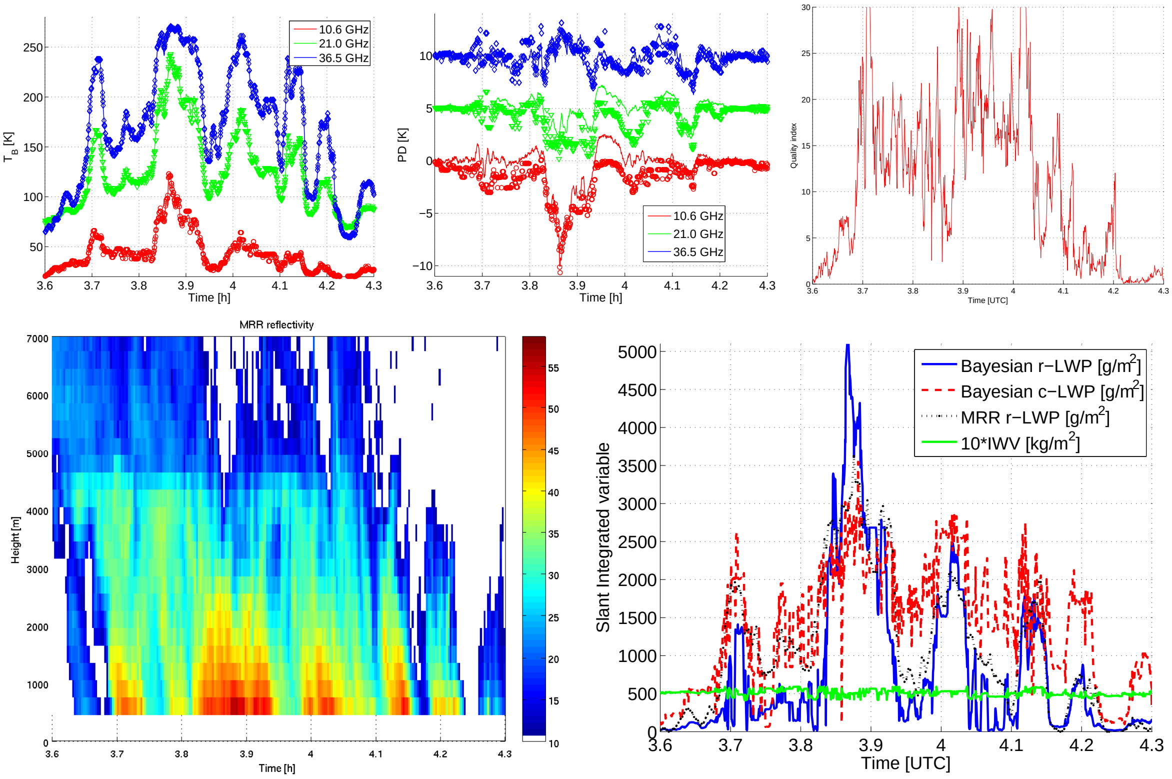

FIG. 19. Case study 01/10/2008 from 3.6 to 4.3.

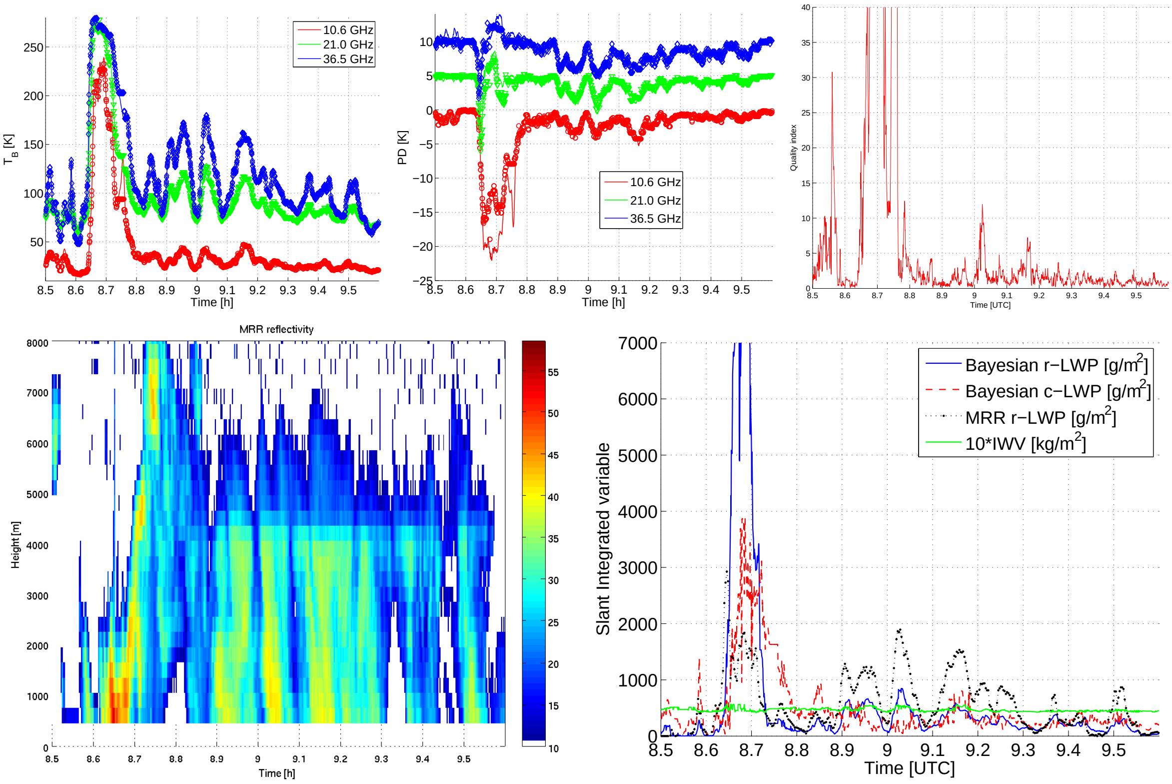

FIG. 20. Case study 01/10/2008 from 8.5 to 9.6.

FIG. 21. Case study 01/10/2008 from 3.6 to 4.3.

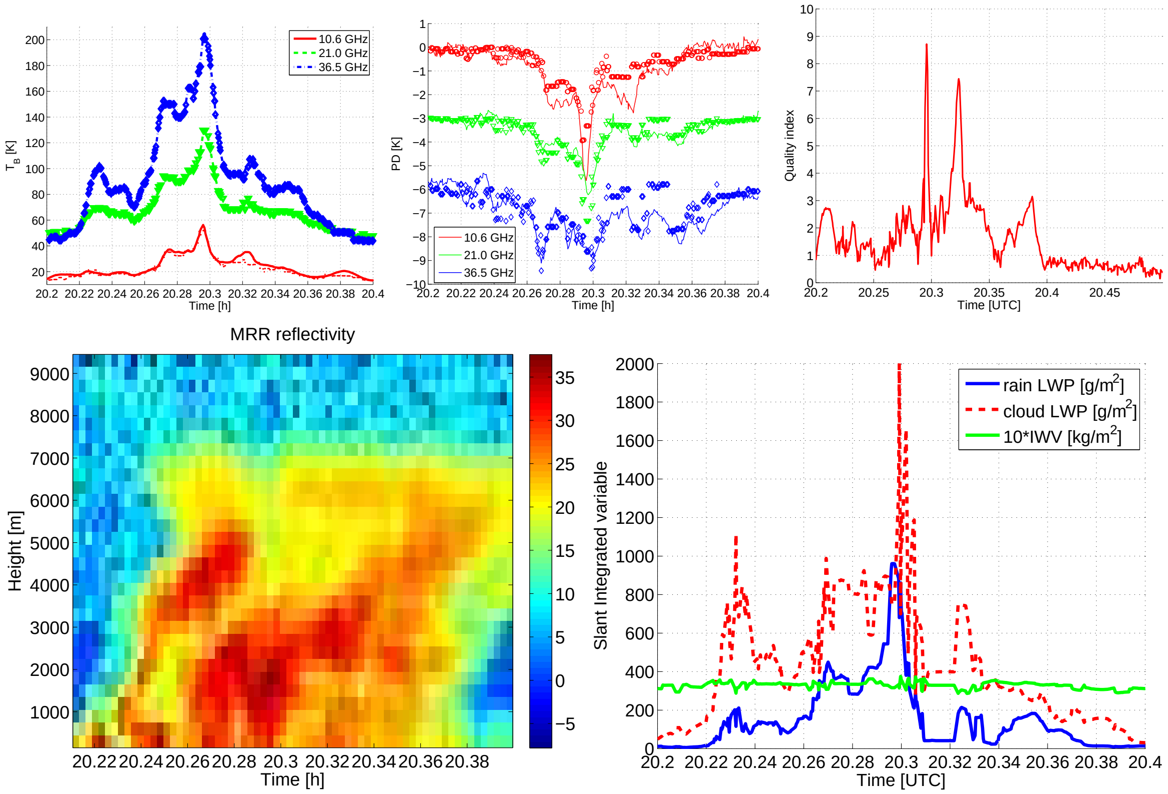

FIG. 22. Case study 1.

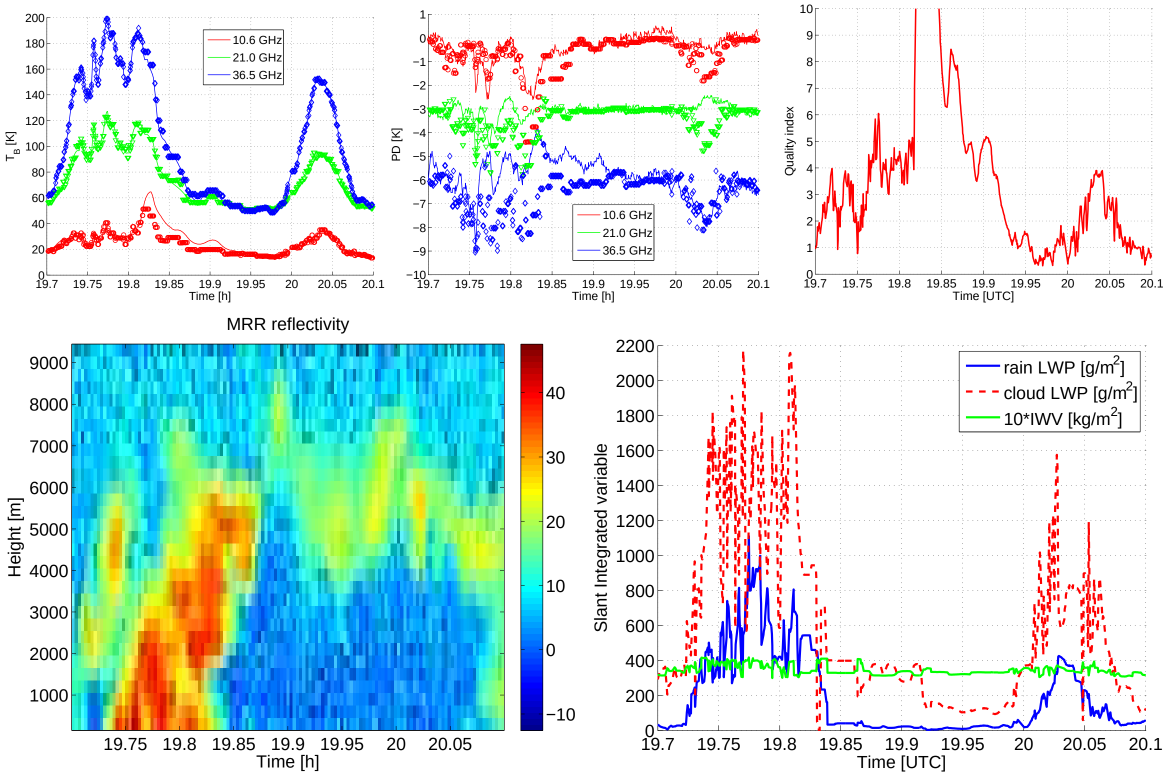

FIG. 23. Case study 2.

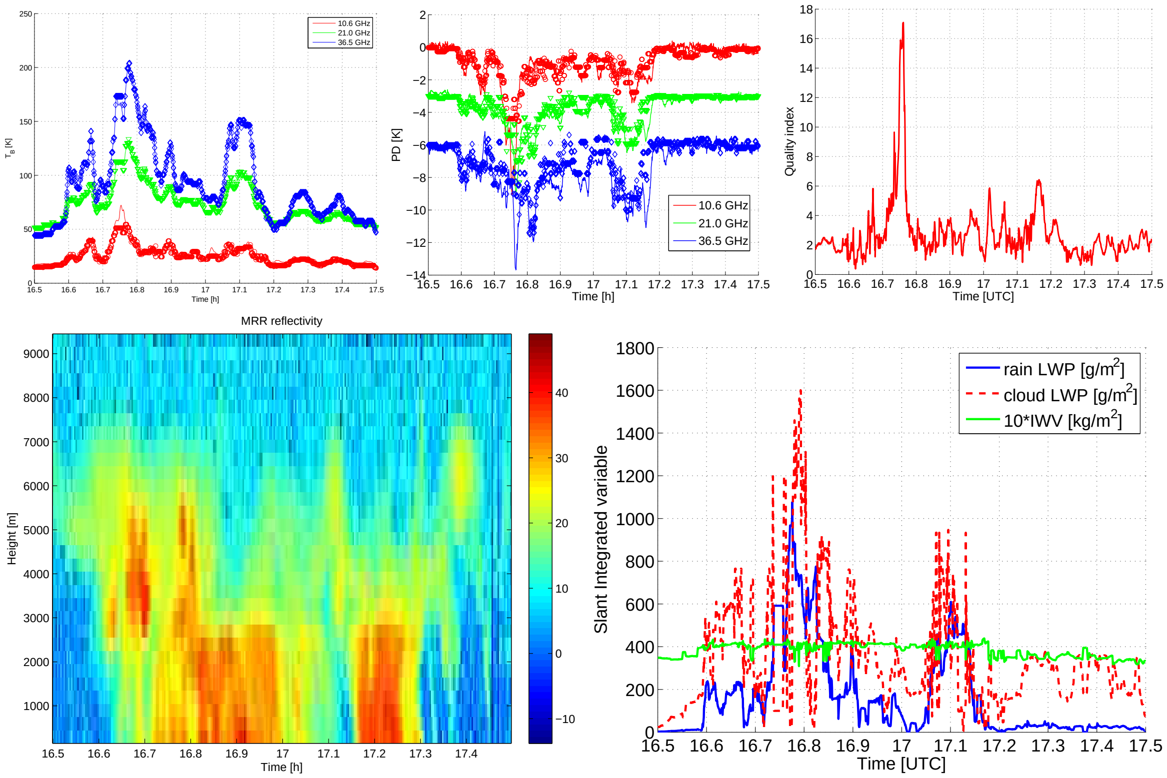

FIG. 24. Case study 3.

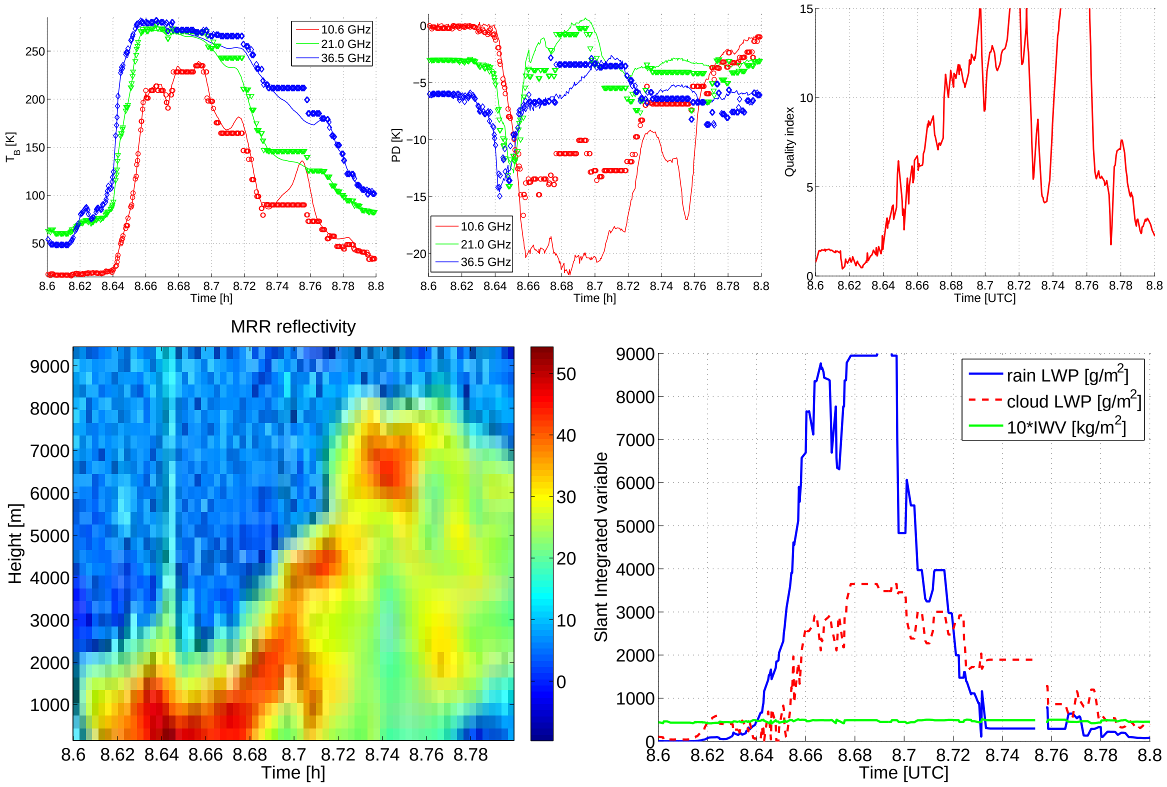

FIG. 25. Case study 4.

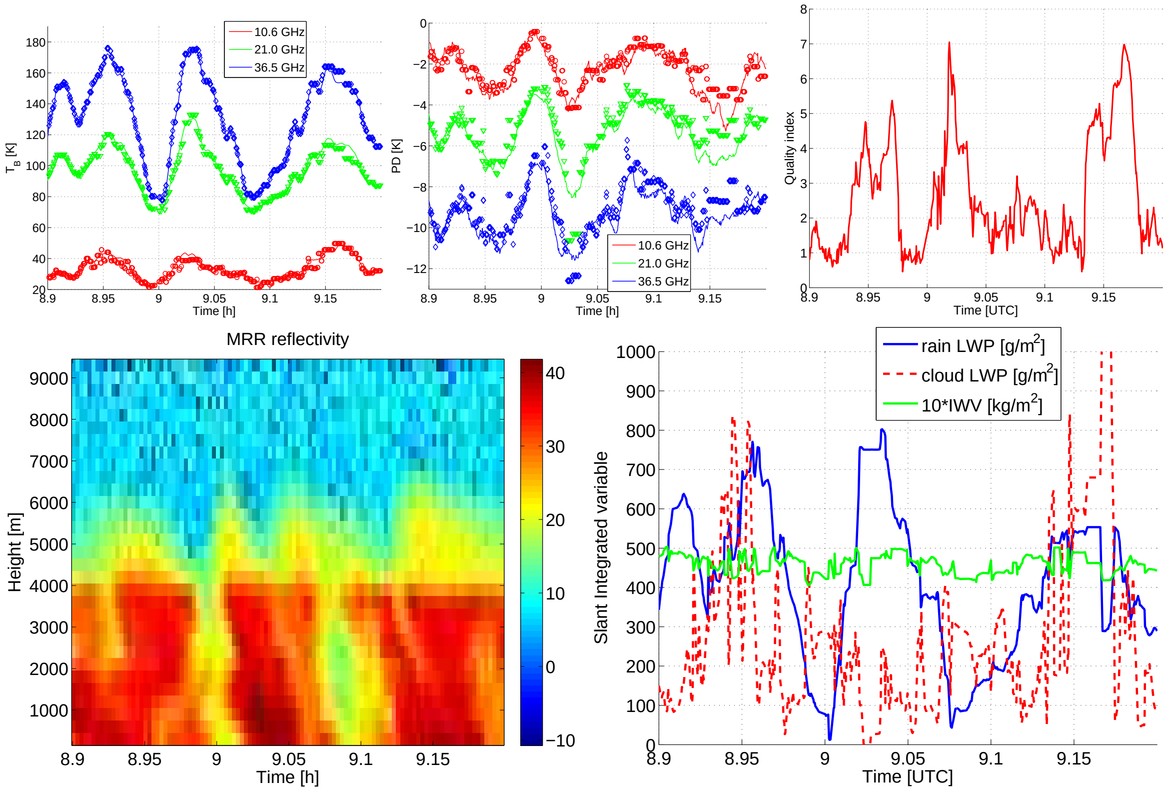

FIG. 26. Case study 5.

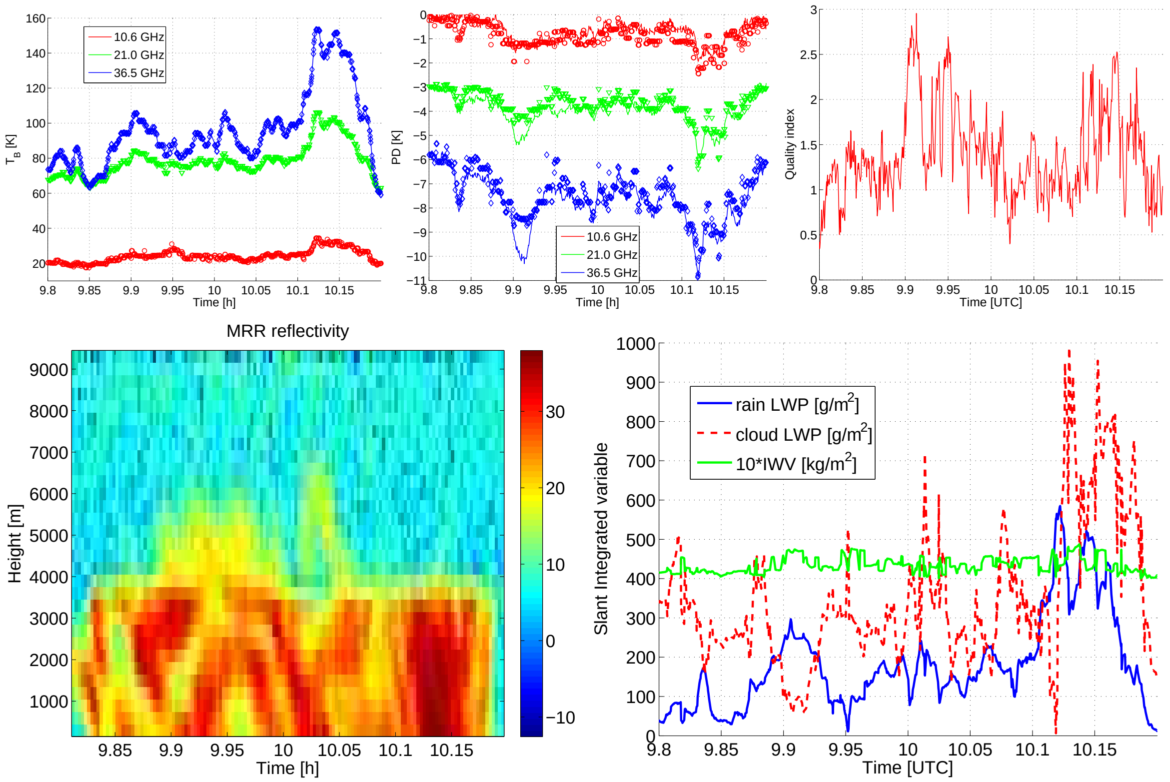

FIG. 27. Case study 6.

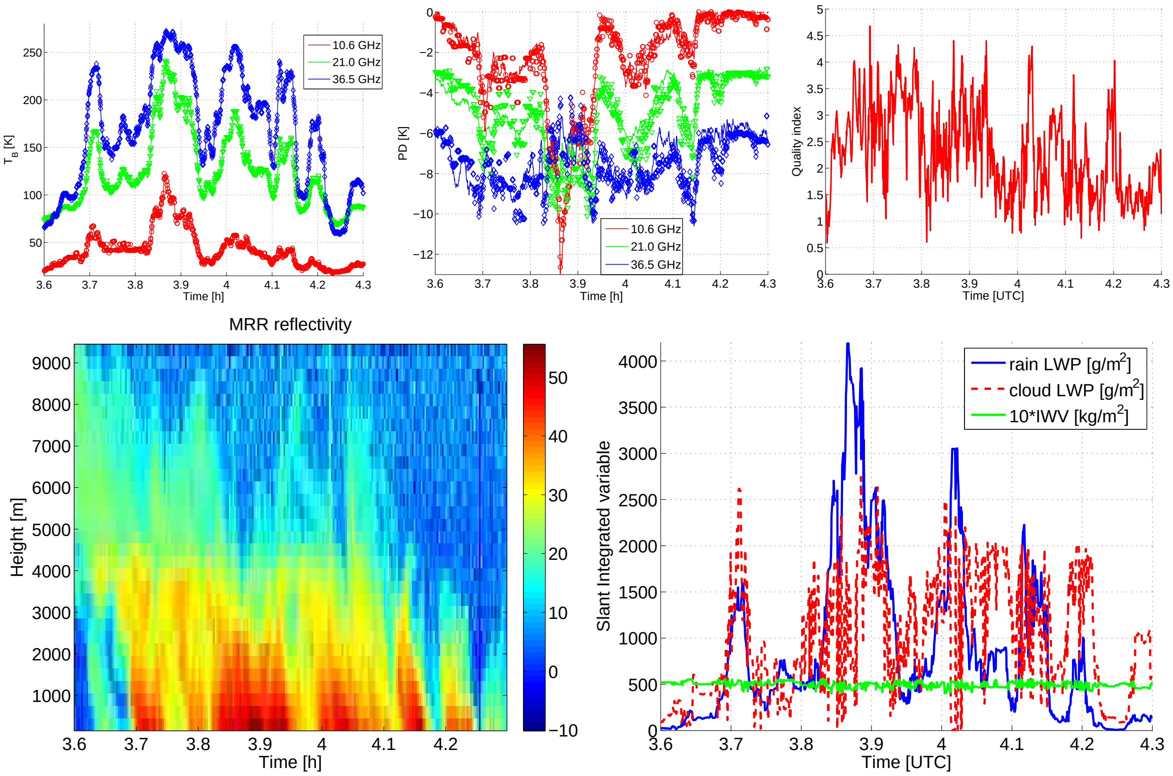

FIG. 28. Case study 7.

List of Tables

TABLE 1. Main characteristics of the ADMIRARI radiometer.

Feature	Specification
Center frequencies [GHz]	$10.65 - 21.0 - 36.5$
Bandwidth [MHz]	400
Minimum integration time [s]	1
System noise temperature	$< 900\ K$ for all receivers
Absolute system stability	$1.0\ K$
Receiver and antenna thermal stabilization	Accuracy $< 0.05\ K$
Antenna beamwidth	$5° - 6.5° - 6.5°$
Side lobes	$< -35dBc \quad < -40dBc \quad < -40dBc$
Cross polarization	
Dicke switching	
Pointing speed	elevation: $3°/sec$; azimuth: $5°/sec$;